This is a repository copy of *In vivo methods and applications of xenon-129 magnetic resonance*.

Version: Published Version

In vivo methods and applications of xenon-129 magnetic resonance

Helen Marshall, Neil J. Stewart, Ho-Fung Chan, Madhwesha Rao, Graham Norquay, Jim M. Wild *

POLARIS, Imaging Sciences, Department of Infection, Immunity and Cardiovascular Disease, University of Sheffield, Sheffield, United Kingdom

Edited by Geoffrey Bodenhausen and David Gadian

ARTICLE INFO

ABSTRACT

Hyperpolarised gas lung MRI using xenon-129 can provide detailed 3D images of the ventilated lung air-spaces, and can be applied to quantify lung microstructure and detailed aspects of lung function such as gas exchange. It is sensitive to functional and structural changes in early lung disease and can be used in longitudinal studies of disease progression and therapy response. The ability of ^{129}Xe to dissolve into the blood stream and its chemical shift sensitivity to its local environment allow monitoring of gas exchange in the lungs, perfusion of the brain and kidneys, and blood oxygenation. This article reviews the methods and applications of *in vivo* ^{129}Xe MR in humans, with a focus on the physics of polarisation by optical pumping, radiofrequency coil and pulse sequence design, and the *in vivo* applications of ^{129}Xe MRI and MRS to examine lung ventilation, microstructure and gas exchange, blood oxygenation, and perfusion of the brain and kidneys.

Contents

* Corresponding author at: University of Sheffield POLARIS, 18 Claremont Crescent, Sheffield S10 2TA, United Kingdom.
    E-mail address: j.m.wild@sheffield.ac.uk (J.M. Wild).

1. Introduction

The noble gas xenon was discovered in 1898 by William Ramsay and Morris Travers, and named from the Greek for "stranger" [1]. Of the nine naturally occurring isotopes of xenon, only ^{131}Xe and ^{129}Xe have non-zero spin, which permits magnetic resonance. ^{131}Xe has spin 3/2 and a nuclear electric quadrupole moment (which dominates spin-lattice relaxation, shortening T_1 to milliseconds), while ^{129}Xe has spin 1/2, no quadrupole moment and a gyromagnetic ratio 3.4 times larger than ^{131}Xe [2]. Xenon is an excellent probe of its chemical environment because it is inert and monatomic with a large spherical electron cloud, the distortion of which affects the NMR chemical shift [3], and ^{129}Xe MR spectroscopy has been employed as such in many studies to determine the properties of a diverse range of microporous solids [2,3].

Laser optical pumping, where circularly polarised light of a suitable wavelength is used to drive the electron spins of certain atoms into non-Boltzmann energy level distributions, was discovered by Kastler in 1950 [4]. In 1960, Bouchiat et al. from the same institute, ENS in Paris, showed that angular momentum could be transferred from the electron spins of optically pumped rubidium vapour to the nuclear spins of ^3He gas [5], the first demonstration of spin-exchange optical pumping (SEOP, see Section 2). The first application of SEOP to ^{129}Xe was demonstrated in 1978 [6] and the technique was further developed by the Happer group at Princeton [7,8], which eventually led to hyperpolarised ^{129}Xe NMR spectroscopy [9] and the first biomedical imaging studies in the 1990s. In 1994 Albert et al. presented the first MR images of hyperpolarised ^{129}Xe in excised mouse lungs [10]. The potential of MR imaging of ^{129}Xe in both its gas-phase and dissolved-phase in the lungs, and subsequent uptake in to the circulatory system, brain and other organs was recognised in the first publications on the subject [10–12]. The first *in vivo* hyperpolarised gas MR images of human lungs were demonstrated by Ebert et al. [13] and MacFall et al. [14] in 1996 using ^3He, and Mugler et al. in 1997 using ^{129}Xe, along with ^{129}Xe spectra of the chest and head [11]. We now perform ^{129}Xe MRI routinely in patients for clinical investigations of lung disease [15].

The noble gases ^3He and ^{129}Xe are particularly suitable as inhaled contrast agents for MR imaging. Noble gases are characteristically safe, non-toxic and unreactive. The ^3He and ^{129}Xe isotopes have a nuclear spin of 1/2, yielding a two-state nuclear energy level structure in the presence of a magnetic field. Crucially, their nuclear polarisations can be dramatically increased using SEOP, facilitating MR signal enhancements of up to 4–5 orders of magnitude. The gyromagnetic ratios of ^3He and ^{129}Xe, pertaining to the available MR signal, are roughly 75% and 25% that of ^1H respectively (Table 1). Helium is almost completely insoluble in the lung parenchyma [16] and blood [17] (Ostwald solubility coefficient < 0.01) due to its tightly bound electron cloud. In contrast, the large, polarisable electron cloud of xenon allows it to dissolve in parenchymal tissue, blood plasma and red blood cells (Ostwald solubility coefficients are: ~0.1 [18], ~0.09 [19] and ~0.2 [19] respectively). It is this non-negligible solubility that permits uptake of xenon into the bloodstream and the subsequent inhibition of N-methyl-D-aspartate receptors in the neuronal cells that is believed to lead to the anaesthetic function of xenon gas [20]. Despite this effect, MR imaging of inhaled ^{129}Xe is safe and well-tolerated in healthy volunteers and patients with pulmonary disease [21,22], including children as young as 6 years old [23]; the ^{129}Xe dose is 1 L or less and breath-holds are short (usually < 16 s) and thus the alveolar concentration is well below the minimum alveolar concentration required to induce anaesthesia. Since the xenon electron cloud is easily distorted, the local magnetic field at the site of the nucleus is readily altered in different chemical environ-

ments. As a result, ^{129}Xe displays a broad range of NMR chemical shift values; of the order of hundreds of ppm when dissolved in various liquids and biological tissues [24].

Due to the higher gyromagnetic ratio and relative ease of polarisation [12], ^3He has historically been the focus of hyperpolarised gas lung MRI research until recently [25,26]. However, the ^3He isotope is rare (being only produced during tritium decay in the nuclear industry) and in recent years has become increasingly scarce and expensive [21,27]. Xenon occurs naturally in the atmosphere in small concentrations (87 ppb), 26.44% of which is constituted by the ^{129}Xe isotope. After extraction from the air via liquefaction and gas separation, xenon gas can be isotopically enriched to increase the ^{129}Xe fraction up to 80–90%. The availability of ^{129}Xe, coupled with progress in ^{129}Xe polarisation and imaging technology, has motivated a shift towards ^{129}Xe for imaging the airspaces of the lungs, and renewed interest in utilising ^{129}Xe for the investigation of gas exchange, lung perfusion, blood oxygenation, and gas uptake in the brain and kidneys.

Hundreds of millions of people worldwide suffer from chronic respiratory diseases including asthma, chronic obstructive pulmonary disease (COPD), cystic fibrosis (CF) and interstitial lung disease (ILD) [28]. Pulmonary function tests are the clinical standard for assessment of lung disease but they only provide global metrics about the function of the lungs as a whole, and are insensitive to early-stage lung disease and subtle changes in lung function. Sensitive, repeatable measures that provide regional information about lung structure and function are essential for the early detection and thorough assessment of spatially heterogeneous lung diseases. High resolution computed tomography (CT) is the gold standard for structural imaging of the lungs; however, it does not provide functional information and entails a significant radiation dose [29], which is a particular problem in high risk patient groups such as pregnant women and children, and in diseases such as CF where longitudinal monitoring is necessary [30]. Ventilation-perfusion scintigraphy and single photon emission tomography (SPECT) are used clinically to image lung ventilation and perfusion function, yet they suffer from poor spatial resolution and the risks of ionising radiation.

Proton (^1H) MRI of the lungs is limited by the low proton density of the lung parenchyma and signal loss due to the magnetic susceptibility differences between the numerous air-tissue interfaces (short T_2^* [31]), with respiratory and cardiac motion presenting additional challenges [32,33]. Advances in scanner hardware

Table 1
Properties of ^1H, ^3He and ^{129}Xe.

Properties	^1H	^3He	^{129}Xe
Isotope abundance (%)[a]	99.99	1.37×10^{-4}	26.44
Nuclear spin[a]	½	½	½
Gyromagnetic ratio (MHz/T)[a]	42.58	−32.43	−11.78
Spin density (10^{19} atoms/cm^3)[b]	6690	2.37	2.37
Chemical shift range (ppm)[c]	~10	~0.8	~250
Self-diffusion coefficient (cm^2/s)[d,e]	2×10^{-5}	2.05	0.062
Free diffusion coefficient (in air) (cm^2/s)[e]	–	0.86	0.14
Ostwald solubility in water[f]	–	0.0096–0.0101	0.083–0.093
Ostwald solubility in blood[f]	–	0.008–0.0104	0.137–0.222

[a] From Ref. [300].
[b] From Ref. [301], ^1H spin density in water, gas spin densities at 1 atm and 37 °C.
[c] From Refs. [24,302], chemical shift offset from gaseous phase resonance (0 ppm).
[d] From Ref. [303], self-diffusion coefficient of water at 25 °C.
[e] From Ref. [176], assuming gas at 1 atm and 37 °C, and an air mixture of 79% N_2 and 21% O_2.
[f] From Ref. [18], for gas at 1 atm and 37 °C.

and pulse sequence design have enabled the assessment of lung morphology (structure) with ^{1}H MRI [32], for example using ultra-short echo-time (UTE) sequences [34,35], which can provide an alternative to CT in some situations [35,36]. Functional lung images can be obtained with ^{1}H MRI [37] either by using external contrast agents which alter T_1 relaxation times, as with dynamic contrast enhanced perfusion imaging [38] and oxygen-enhanced imaging [39], or by using the modulation of the proton signal caused by respiratory and cardiac motion to infer lung ventilation and perfusion indirectly [40]. While these techniques offer the advantage of functional imaging without the need for additional hardware, hyperpolarised gas MRI allows direct imaging of the inhaled contrast agent and can be tuned to different aspects of lung function, and also probe more distal organs in the case of hyperpolarised [129]Xe MRI.

This review will focus on the methodology and applications of hyperpolarised [129]Xe MRI and MRS, covering: 1. optical pumping physics, 2. imaging physics considerations, 3. radiofrequency coils, 4. ventilation imaging, 5. diffusion-weighted imaging and modelling, 6. dissolved-phase [129]Xe lung MRI and MRS, 7. [129]Xe dissolved in human blood, and 8. imaging inhaled [129]Xe beyond the lungs.

2. Spin-exchange optical pumping physics

While it is possible to perform MR imaging on thermally polarized (i.e. non-hyperpolarised) [129]Xe (for example in high-pressure cells for the purpose of quality control testing), the low density of gases compared to protons in water and biological tissue renders the NMR signal of this non-hyperpolarised [129]Xe too low for *in vivo* lung imaging in practice. To overcome this inherent sensitivity limitation, the nuclear spin polarisation of [129]Xe can be enhanced beyond its thermal equilibrium Boltzmann polarisation, resulting in a "hyperpolarised" (HP) [129]Xe nuclear spin system.

Although HP [129]Xe can be produced by dynamic nuclear polarisation [41], the technique most commonly used to hyperpolarise [129]Xe nuclei for MR applications is rubidium (Rb) spin-exchange optical pumping (SEOP) [6,8]. SEOP is a two-step physical process involving (i) polarisation of the valence electrons in Rb vapor through absorption of circularly polarised light (optical pumping) and (ii) collisional energy transfer from the polarised Rb electrons to [129]Xe nuclei (spin exchange) – see Fig. 1. SEOP with [129]Xe generally requires relatively low densities of xenon gas (0.01–0.25 xenon partial pressure) owing to high destruction rates of Rb electron polarisation at elevated xenon concentrations [42]. The gas mixture used for [129]Xe-SEOP is therefore diluted with a buffer gas – typically either a [4]He-N_2 mixture or pure N_2 gas – which also serves to (i) prevent emission of non-circularly polarised photons during electronic Rb relaxation [43][1]; and (ii) pressure broaden the Rb D$_1$ linewidth, which improves photon absorption efficiency [44].

Typically, one of two approaches to produce HP [129]Xe with SEOP is used: the "stopped-flow (SF)" (also known as "batch") mode [45–47,309], in which higher-density xenon gas mixtures (up to 25% xenon concentration) are dispensed directly from the SEOP cell; and (ii) the "continuous-flow (CF)" mode [48–54], in which a lower-density xenon gas mixture (1–3% xenon concentrations) is allowed to flow through the SEOP cell over a period of time, and xenon is cryogenically separated from the buffer gases. While higher [129]Xe polarisation values have been reported in SF-SEOP [46,47,55,56], the xenon production rates are generally of the order of 100 mL/h, with the highest observed being ~1000 mL/h [56],

which can be compared to >1000 mL/h characteristic of CF-SEOP [48,49,51]. There is therefore a trade-off between the achievable [129]Xe polarisation and the xenon volume production rate when considering SF- and CF-SEOP methods for a given application. For example, for MR applications of HP [129]Xe in a clinical setting, CF-SEOP is most suitable, as it is critical to have a large volume production rate in order to enable large volumes of [129]Xe to be produced on demand; whereas for applications where high-throughput and large volumes of xenon are not required (e.g. *in vitro* NMR [129]Xe applications), SF-SEOP is more suitable.

A useful metric to evaluate [129]Xe polariser performance is the dose equivalent rate, $DE_{rate} = fQ_{Xe}P_{Xe}$, which expresses the xenon volume production rate (Q_{Xe}) of 100% polarised [129]Xe and 100% isotopically enriched xenon, where f is the isotopic fraction of [129]Xe and P_{Xe} is the [129]Xe nuclear spin polarisation [58]. Through employment and optimization of a large SEOP cell (3530 mL volume), a high HP [129]Xe production efficiency on a continuous-flow polariser has recently been reported [59], with a DE_{rate} of 1013 mL/h. This has enabled routine clinical lung MRI with hyperpolarised [129]Xe doses available on demand at run time as well as high signal-to-noise ratio (SNR) [129]Xe MRI of the human brain [60–62] and kidneys [63].

3. Imaging physics considerations

The induced hyperpolarisation of [129]Xe is not renewable; that is, the polarisation relaxes by longitudinal (T_1) relaxation to the equilibrium (Boltzmann) polarisation, which is a factor of 10^4-10^5 times lower than the induced hyperpolarisation. This decay is accelerated when applying radiofrequency (RF) pulses. Thus, the longitudinal magnetisation of [129]Xe decays continuously from its maximum, M_0, according to RF excitation and T_1, described by the following equation, assuming a constant flip angle, θ, and gradient spoiling between RF pulses [64]:

$$M_n = M_0 exp\left(-\frac{(n-1)TR}{T_1}\right)cos^{n-1}(\theta) \qquad (1)$$

where M_n is the longitudinal [129]Xe magnetisation after n RF pulses and TR is the inter-pulse repetition time.

The intrinsic gaseous T_1([129]Xe) is of the order of hours at room temperature, measured at a Xe density of 0.15 amagat [65]. However, the decay of hyperpolarised [129]Xe signal in the lungs is orders of magnitude more rapid (T_1([129]Xe) approximately 20 s [66]), primarily due to the presence of paramagnetic oxygen. Intermolecular dipolar coupling between molecular oxygen and the [129]Xe nuclei leads to a linear dependence of the longitudinal relaxation rate $1/T_1$([129]Xe) of the gas on the partial pressure of oxygen (pO$_2$) [67]. The T_2*([129]Xe) value in the alveoli is considerably longer than lung T_2*(^{1}H) values (approximately 1.4 ms at 1.5 T [31]), and is influenced by lung inflation level (T_2*([129]Xe) = 25 ms at FRC + 1 L and 52 ms at TLC at 1.5 T) as well as B_0 strength (18 ms at FRC + 1 L and 24 ms at TLC at 3 T) [68]. As the acquired MR signal is boosted by hyperpolarisation of the gas, image SNR is largely independent of B_0 at the current clinically-used magnetic fields (1.5 T and 3 T) [68]; however, increased T_2*([129]Xe) dephasing in regions of B_0 field inhomogeneity such as near blood vessels and the diaphragm is evident at 3 T.

To conserve the non-renewable hyperpolarised gas signal as much as possible, low-flip angle gradient echo and steady-state free precession sequences form the foundation of hyperpolarised gas pulse sequence design [64]. As the available magnetisation is partly depolarised by each RF pulse, RF depolarisation filters are imposed in *k*-space such that an image phase encoded with sequential ordering in Cartesian space has lower SNR but higher spatial frequency detail than an otherwise identical acquisition
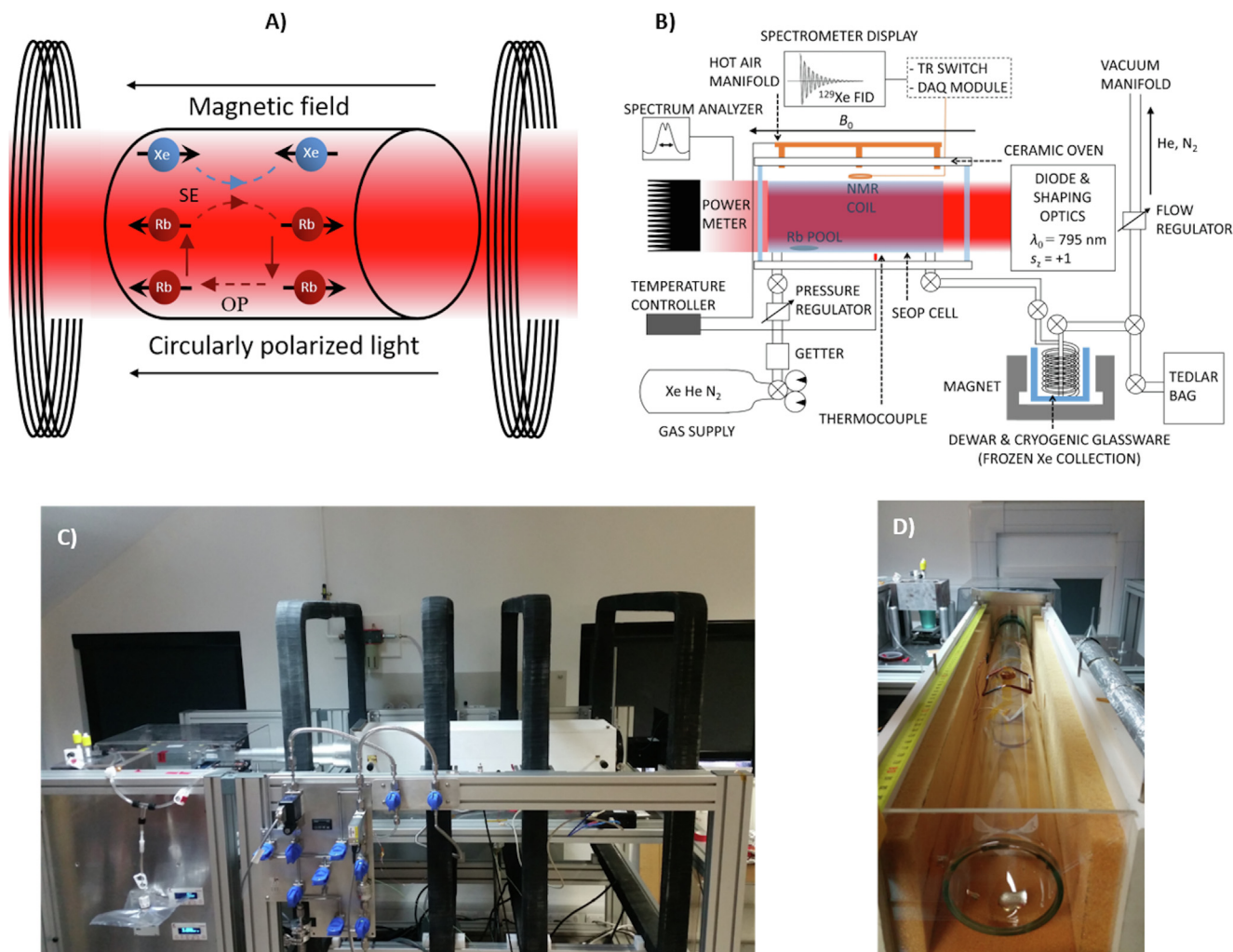
---

[1] Energy is transferred into the rotational/vibrational levels of the N_2 molecules, resulting in non-radiative electronic decay.

Fig. 1. Optical pumping. (a) Simplified conceptual picture of Rb-^{129}Xe spin-exchange optical pumping (SEOP). SEOP is a two-step process involving (i) the spin polarisation of Rb valence electrons through optical pumping of Rb vapour with circularly polarised light resonant with the Rb D_1 transition and (ii) transfer of the Rb electron polarisation to the nuclei of ^{129}Xe via spin-exchange collisions. The black arrows depict the polarisation of the Rb electron and ^{129}Xe nuclear spin states. OP and SE represent optical pumping and spin-exchange interactions, respectively. (b) Schematic of the key functional components of a continuous-flow Rb-^{129}Xe polariser, adapted with permission from [59]. A stopped–flow set-up is essentially the same without the need for a cryostat and magnet (see bottom right). (c) Photo of ^{129}Xe spin-exchange optical pumping polariser located at the POLARIS laboratory, University of Sheffield. (d) Ceramic oven containing V = 3530 mL SEOP (7.5 cm diameter, 80 cm length) cell without the lid. The pool of rubidium is visible at the cell gas entrance (bottom of photo). Incident laser light P = 150 W (BrightLock 200 W, QPC, CA, USA), 794.77 nm wavelength. Gas mixture throughout: 3% Xe, 87% He, 10% N_2.

using centric Cartesian phase encoding [69]. Variable flip-angle schemes have been proposed to counteract this effect [64,70,71], where the flip angle is stepwise increased during image acquisition to maintain constant transverse magnetisation, but in practice these schemes can be difficult to implement in a robust fashion due to B_1 inhomogeneity [72] and RF power limitations considering the low gyromagnetic ratio of ^{129}Xe. Non-Cartesian k-space acquisition trajectories lead to different RF k-space depolarisation filters, causing artefacts and loss of spatial resolution, which can be compensated for after signal acquisition or mitigated by using non-sequential acquisition order to distribute the effects of the filter more evenly over k-space [73,74].

In 2D hyperpolarised gas imaging, the distribution of effective flip angles over a realistic selected slice thickness causes the uniformity of the slice profile to decrease with increasing phase encoding number [69,72]. The smaller flip angles experienced at the edges of the slice profile deplete the longitudinal magnetisation of ^{129}Xe gas at a slower rate than in the slice centre, meaning that the later phase encodes are more heavily weighted by signal from the slice edges. In addition, diffusion of "fresh" hyperpolarised gas from outside the selected slice that has not been affected by the RF pulses adds to the in-slice signal throughout the acquisition. These effects can cause errors in slice-selective techniques which use temporal signal decay to calculate parameters such as the partial pressure of oxygen in the lung (pO_2) [75].

Diffusion of hyperpolarised gas within the lung airspaces during imaging limits the achievable spatial resolution and leads to signal attenuation resulting from the imaging gradients, reducing the effective transverse relaxation time, though this effect is minor compared to RF depolarisation [69] and less pronounced for ^{129}Xe compared to ^{3}He due to its lower diffusion coefficient. The confining structure of healthy alveoli limits the distance that gas molecules can travel but in some diseases such as emphysema the alveolar walls are damaged or destroyed, allowing increased diffusion and therefore exacerbating related effects [76]. However, the sensitivity of hyperpolarised gas diffusion to its surrounding structural environment can be exploited as a unique means to obtain information about lung microstructure, as addressed in Section 6.

3.1. Pulse sequences

Whilst 2D spoiled gradient echo (SPGR) scans acquired with contiguous slices spanning the whole of the lungs are robust, signal-to-noise benefits can be obtained with balanced steady-state sequences that exploit the long T_2 of hyperpolarised gases by recycling the transverse magnetisation remaining at the end of each repetition time [77,78]. However, these sequences are sensitive to off-resonance effects, which can lead to banding artefacts in regions of poor B_0 homogeneity (e.g. close to the diaphragm); these effects are more pronounced at higher field strengths [78]. SNR gains may also be realised by using 3D gradient echo acquisitions in place of slice-selective 2D equivalents [79], though increased sensitivity to motion can cause image blurring.

Non-Cartesian k-space acquisition schemes such as radial [80] and spiral [81,82] enable time-resolved imaging of ^{129}Xe gas with high temporal resolution, to investigate ventilation dynamics. Spiral trajectories can achieve high temporal resolution by an optimal k-space encoding efficiency, whilst the temporal resolution of radial encoding is maximised by sharing radial views in a sliding window reconstruction. In addition, centre-out (ultra-short echo time (UTE)) radial and spiral trajectories sample the centre of k-space (k_0, which is representative of the total magnetisation in the imaging volume) every TR. Thus, the time-dependence of the magnitude of the k_0 point is intrinsically sensitive to magnetisation dynamics; this idea can be used to correct hyperpolarised ^{129}Xe images for the filtering effects of RF-induced depolarisation [74]. This approach was recently extended to allow regional mapping of the RF depolarisation (and, therefore, of the flip angles) by using a keyhole reconstruction technique, wherein radial datasets are divided into two temporally resolved "keys" post-acquisition [83]. However, despite the advantages for monitoring of ^{129}Xe magnetisation dynamics, the SNR of 3D radial ^{129}Xe MR images has been reported to be lower than a dose equivalent 2D multi-slice SPGR sequence [58]. Novel trajectories for hyperpolarised ^{129}Xe MRI, including spiral-based techniques for efficient encoding of 3D k-space such as Fermat Looped ORthogonally Encoded Trajectories (FLORET) [84], are a subject of keen interest. 3D radial UTE sequences show good promise for imaging of pulmonary gas exchange with ^{129}Xe MRI, where short $T_2^*(^{129}$Xe$)$ is a limiting factor (as discussed in Sections 3.3 and 7).

3.2. Acceleration techniques

Due to the time-dependence of the magnetisation, MRI with hyperpolarised gas is particularly suitable for image acceleration techniques which reduce the number of RF pulses required to acquire an image, such as parallel imaging [85,86] and compressed sensing [87]. As fewer RF pulses are required, higher flip angles can be used to acquire data with increased signal [88–90]. Thus, for hyperpolarised gases, there is no SNR penalty proportional to $1/\sqrt{R}$ as is observed in thermally-polarised parallel imaging (where R is the "acceleration" factor by which the number of phase encoding steps is reduced compared to full Fourier encoding) [86], enabling high acceleration factors with little degradation of the image quality [90–93]. Compressed sensing has the advantage that it does not require multiple receiver coils and has been successfully implemented to accelerate ^{129}Xe imaging and enable: acquisition of ^{129}Xe images and ^{1}H anatomical MR images in a single breath-hold which aids their registration [94]; high-resolution multiple b-value diffusion-weighted imaging [95,96]; increased temporal resolution in dynamic ^{129}Xe imaging [94,97]; and combined acquisition of diffusion-weighted and gas-exchange ^{129}Xe imaging in a single breath-hold [98]. Furthermore, prior knowledge can be used to improve image reconstruction and achieve higher acceleration, for instance by using knowledge of the magnetisation decay or

structural information from ^{1}H MR images [99], or the sparsity of complex difference images for gas flow applications [100]. As hyperpolarised gas MR images are inherently sparse, it is possible to simplify the reconstruction process by skipping the sparsifying transformation step in some cases [101].

3.3. Additional considerations for MR imaging of ^{129}Xe in the "dissolved phase"

Upon inhalation, xenon partially dissolves in the lung parenchymal tissue and blood plasma (Ostwald solubility coefficient ~0.1) and red blood cells (0.27) [102]. In the lungs, there is a distinct downfield chemical shift of ^{129}Xe dissolved in the lung parenchymal tissue and blood plasma (referred to as TP or "barrier" by some research groups) of 197 ppm and in the red blood cells (RBCs) of 216–222 ppm, (with respect to the resonance of gaseous-phase ^{129}Xe in the alveolar airspace) – see Fig. 4b and Table 2. By acquiring MR signals on a timescale similar to that during which ^{129}Xe exchanges between these compartments, the chemical shift phenomenon can be exploited to quantitatively assess pulmonary gas exchange function. This so-called "dissolved-phase" ^{129}Xe gas exchange MRS/MRI is a subject of active research (see Section 7).

Dissolved-phase ^{129}Xe MRS/MRI presents several additional challenges when compared to conventional hyperpolarised MRI of alveolar ^{129}Xe gas. Firstly, the complex magnetic environment of the lungs and large susceptibility gradients between airspace and tissue lead to extremely short transverse relaxation times of ^{129}Xe dissolved in the lung parenchyma and blood ($T_2^*(^{129}$Xe$) \lesssim$ 2 ms). Therefore, dissolved-phase ^{129}Xe signal is usually acquired as a free induction decay or echo with very short echo time. In light of the benefit of longer $T_2^*(^{129}$Xe$)$ values [103], considerable development work for dissolved ^{129}Xe MRI/MRS in humans has been performed at a field strength of 1.5 T ($T_2^*(^{129}$Xe$)$ ~2.2 ms [104]), and this has recently been shown to be translatable to 3 T (T_2^* $(^{129}$Xe$)$ ~1.1 ms) [105]. In addition, upon diffusing into the lung parenchyma, ^{129}Xe rapidly exchanges between the parenchyma and pulmonary capillaries (typical time constant for airspace to capillary transfer <100 ms [106,107]), and within the capillaries, ^{129}Xe exchanges between plasma and RBCs on a timescale of 12 ms [108]. Dissolved phase ^{129}Xe MRI/MRS is further complicated by the low signal (~2% of that of the gaseous phase ^{129}Xe), which arises from the low tissue/gas volume ratio (~0.2) and low solubility of xenon in parenchymal tissue (0.1). Fortunately, the gaseous phase ^{129}Xe acts as a reservoir to replenish dissolved-phase magnetisation after its depolarisation and thus a relatively high flip angle can be applied to the dissolved phase. This necessi-

Table 2
^{129}Xe chemical shifts in somatic substances.

Solvent	Chemical Shift (ppm)
Distilled water	190[a]
Saline (0.9% NaCl)	194[b]
Olive oil	198[c]
Rat adipose tissue	191[d]
Blood plasma	194[a]
	197[e]
Erythrocytes (red blood cells)	216[a]
	222[e]
Perfluorooctyl bromide emulsion (PFOB)	106[f]

The offset is expressed in parts per million (ppm) from the gaseous-phase ^{129}Xe resonance (0 ppm).
[a] From Ref. [304].
[b] From Ref. [305].
[c] From Ref. [24].
[d] From Ref. [220].
[e] From Ref. [223].
[f] From Ref. [306], PFOB is a blood substitute.

tates careful design of RF excitation pulses to selectively excite the dissolved phase ^{129}Xe whilst minimising off-resonant excitation of the gaseous phase reservoir [109,110]. Despite these challenges, the longitudinal relaxation time of ^{129}Xe gas in the alveolar spaces (T_1(^{129}Xe) ~ 25 s at 1.5 T [68]) is longer than that of a typical breath-hold scan duration, and in blood (T_1(^{129}Xe) ~ 6–13 s [111–113]) is sufficient to enable detection in distal organs such as the brain [114,115] and kidneys [63] (see Section 9).

4. Radio frequency coils

The low gyromagnetic ratio (−11.78 MHz T^{-1}), unit dielectric constant (1.00126) and nonconductive properties of gaseous ^{129}Xe predominantly define the design considerations for radio frequency (RF) coils [116]. Due to the low Larmor frequency of ^{129}Xe (17.66 MHz at 1.5 T and 35.33 MHz at 3.0 T) when compared to ^{1}H (63.83 MHz at 1.5 T and 127.6 MHz at 3.0 T), the Ohmic loss of the RF coil is lower, as it is proportional to the square root of the resonant frequency ($\sqrt{\omega}$) [117]. Radiation loss is negligible as the dimensions of the RF coil are very small when compared to the Larmor wavelength, diminishing the likelihood of magnetic dipole radiation. Dielectric losses due to capacitive coupling and dissipation due to inductive coupling with ^{129}Xe as an NMR sample in situ in a RF coil are nil due to the near unity dielectric constant and the lack of conductivity [118–122], and thus, ^{129}Xe does not contribute to sample-dominated losses [123]. Hence, the efficiency of RF transmission and detection for ^{129}Xe is mainly determined by the filling factor [124] of the RF coil. However, tissues in organs containing ^{129}Xe such as the lungs, brain and kidneys do contribute to the sample-dominated loss by inductive coupling, which is proportional to the square of the resonant frequency (ω^2) [120–122]. The achievable sample loss, measured as a ratio ($Q_{Coil} = Q_{Loaded} \cdot Q_{Unloaded}^{-1}$) of the quality factor with (Q_{Loaded}) and without ($Q_{Unloaded}$) the sample in situ [123], which measures coupling of an RF coil to the sample, is proportional to $R\omega^{\frac{3}{2}} + 1$ [120], where ω is the resonant frequency and R is a constant that depends on inductive coupling and conductive losses. Although Q_{Coil} does not provide a direct measurement of SNR, by estimating the inductive coupling of the RF coil with the sample, it provides an indication of the sensitivity of the RF coil to the anatomy or airspace containing ^{129}Xe. Thus, in order to optimise a ^{129}Xe RF coil for efficiency and SNR, both the filling factor [124] that confirms sensitivity towards the sample space and sample losses that confirm sample domination [123,125,126] should be optimised. In contrast, for conventional RF coils for proton imaging, optimising for sample-loss implicitly optimises filling factor as the same sample both induces losses and generates NMR signal.

As the Larmor frequency of ^{129}Xe is much lower than that of ^{1}H, receive-only RF coil arrays with a large number of channels, which are adapted to the subject with close proximity, provide relatively moderate improvements in SNR over transceiver RF coils [92] compared to those seen for ^{1}H receiver RF coil arrays [127,128]. Thus, high density receiver RF coil arrays for ^{129}Xe [93] primarily serve the purpose of accelerating imaging by benefitting from the fact that for hyperpolarised gases, the SNR can be preserved when under-sampling k-space while increasing the flip angle, which is made possible by the reduced number of RF pulses [91–93,129]. A recent approach to increase the SNR of a receiver RF coil array for ^{129}Xe was to optimise the filling factor and reduce conductive loss by using superior grade copper [60].

Transmit RF coils for ^{129}Xe lung MRI of birdcage topology are large enough to fit an adult human torso and typically have an elliptical or oval shape in the transverse plane orthogonal to B_0 conforming to the patient table and magnet [93,130,131]. The design of a non-cylindrical birdcage is determined by conformal mapping and modal mesh currents [130,131]. B_1^+ homogeneity (i.e. standard deviation of B_1^+ field amplitude) of 7% is achievable, which may be compared to 16% achieved with a flexible dual Helmholtz coil [130]. However, the latter has advantages in terms of comfort and ease of patients' entry into the magnet. In contrast, transmit RF coils of birdcage topology for ^{129}Xe brain MR imaging have a cylindrical shape with B_1^+ homogeneity of 6.5% [60,114].

In clinical practice, it is often necessary to acquire spatially concordant ^{1}H images along with the ^{129}Xe images, for planning, structure-function assessment and to arrive at quantitative measures such as ventilation defect percentage [132–136]. For ^{129}Xe brain MRI, complementary ^{1}H images of the brain can be acquired in a separate session with separate RF coils, and since the human head is rigid, the images can be easily co-registered without image manipulation [60,114]. However, in order to co-register ^{1}H and ^{129}Xe images of the lungs, it is essential to acquire both image sets in the same lung inflation state, and preferably back-to-back in the same breath-hold, ^{129}Xe imaging followed by ^{1}H imaging [94,135–138]. To achieve this the RF coil(s) can be enabled for multi-nuclear lung imaging [139] using multi-tuned RF coils [140–143], multiple electrically-isolated RF coils [136,144,145] or switchable-resonance RF coils [146,147], or otherwise the scanner's body ^{1}H RF coil can be used along with a dedicated RF coil for ^{129}Xe which is electrically isolated for ^{1}H [132–137].

5. Ventilation imaging

MR imaging of gaseous-phase HP ^{129}Xe during a static breath-hold can provide detailed 3D images of the ventilated airspaces of the lungs. Ventilation function can be quantified using several approaches, which typically require the acquisition of co-registered ^{1}H anatomical images along with ^{129}Xe ventilation images in order to derive the total lung volume. The most commonly used metric of ventilation is the ventilation defect percentage (VDP) – the percentage of the lung volume with low or no signal on ^{129}Xe ventilation MRI, and its counterpart ventilation volume percentage (VV% = 100 – VDP) [133,148–154]. ^{129}Xe VDP is reproducible [155–158], increases with age [149,151,155] and correlates with pulmonary function tests [155–157,159]. Regional ^{129}Xe ventilation metrics have shown significant correlation with ventilation/perfusion SPECT and CT percentage emphysema [160], and CT-based surrogates of lung ventilation [161]. In addition, ventilation image signal intensity can be classified into clusters of graded ventilation [148,150,151,154] and its regional coefficient of variation can be calculated to assess ventilation heterogeneity [162,163].

^{129}Xe ventilation imaging is extremely sensitive to obstructive lung disease,[2] exhibiting increased ventilation heterogeneity and VDP in patients with chronic obstructive lung disease (COPD) [157,159], asthma [155,163,164,311], cystic fibrosis (CF) [156,165–167] and non-small-cell lung cancer [157], compared to healthy volunteers (Fig. 2). Studies in children and young adults with CF [156,165,167], lymphangioleiomyomatosis [168] and following allogenic haematopoietic stem cell transplantation [169], where ventilation defects were detected in patients with clinically-normal spirometry (i.e. indicating that ^{129}Xe ventilation MRI is sensitive to "sub-clinical" disease), highlight the sensitivity of ^{129}Xe ventilation imaging to early-stage lung disease, which could allow earlier interventions to impede disease progression. In children and young adults with CF, ventilation defects are often not associated with structural abnormalities evident on ^{1}H ultra-short echo time MRI [167], suggesting that early functional deficits may be detected prior to structural damage.

---

[2] Obstrctive lung diseases prevent patients from exhaling completely while restrictive lung diseases cause patients to have difficulty expanding their lungs fully.

In addition to early sensitivity, the non-ionising nature of [129]Xe ventilation MRI, coupled with its safety and tolerability in adults and children [21–23], make it well suited for longitudinal follow-up post-intervention scans. [129]Xe ventilation MRI response to therapy has been demonstrated in: patients with asthma after bronchodilator inhalation [163] and bronchial thermoplasty [312], children with CF after pulmonary exacerbation and subsequent treatment with intravenous antibiotics [170], patients with CF after acute maximal exercise [313], patients with bronchial stenosis after airway stent placement [171], and a patient with adenocarcinoma after radiotherapy [172]. In a study monitoring response to antibiotics in children with CF, [129]Xe VDP showed the largest relative improvement of all outcome measures [170], and [129]Xe ventilation MRI has been shown to be a sensitive method to assess longitudinal lung disease in children and adults with CF [158,314]. Increased [129]Xe ventilation heterogeneity at low lung inflation levels, consistent with airway closure, has been noted in healthy elite divers who were able to exhale beyond the residual volume of the lungs [173], and in healthy volunteers [174], emphasising the need to control for lung inflation level to ensure reliable longitudinal ventilation imaging.

[129]Xe and [3]He ventilation images of the same patient are visually similar [157,159,161] (Fig. 2a), although greater ventilation abnormalities (and quantitatively higher VDP) are often evident on [129]Xe images when compared to [3]He images [157,159,163,175], likely due to the lower diffusion coefficient of [129]Xe in air [176]. Similarly, the lower diffusion coefficient of [129]Xe in air limits the sensitivity of time-resolved [129]Xe ventilation imaging for the detection of delayed and collateral ventilation

observed in patients with severe COPD using [3]He MRI [177,178]. While ^{1}H anatomical imaging is often performed in a separate breath-hold, advances in multi-nuclear hardware and compressed sensing have made imaging [129]Xe and ^{1}H within the same breath-hold possible [94,136,138]. This provides spatially and temporally registered images of complementary lung ventilation and structure.

Rapid time-resolved [129]Xe imaging allows visualisation of ventilation and measurement of spatially resolved signal-time curves during a breathing cycle [82,97], and velocity mapping of gas flow in the major airways [100]. [129]Xe multiple-breath washout imaging, where dynamic ventilation imaging is performed over several breathing cycles provides spatially resolved information about gas washout complementary to the clinical multi-breath washout pulmonary function test. This provides fully quantitative imaging of fractional ventilation (the turnover of gas per breath), and has been demonstrated in healthy adults [179] and a 9-year-old child with CF [158].

6. Diffusion weighted imaging and modelling

The relatively high diffusivity of hyperpolarised noble gas isotopes (Table 1), in comparison to protons in water molecules, is ideally suited for pulsed gradient echo diffusion-weighted MRI, where the random Brownian motion of inhaled [129]Xe or [3]He gas atoms in the acinar airspace is used to probe the underlying acinar microstructure. The free diffusion coefficient (D_0) of [129]Xe in air (at atmospheric pressure and body temperature) is 0.14 cm^2/s [176], and over a time-scale of several milliseconds (Δ), [129]Xe gas atoms
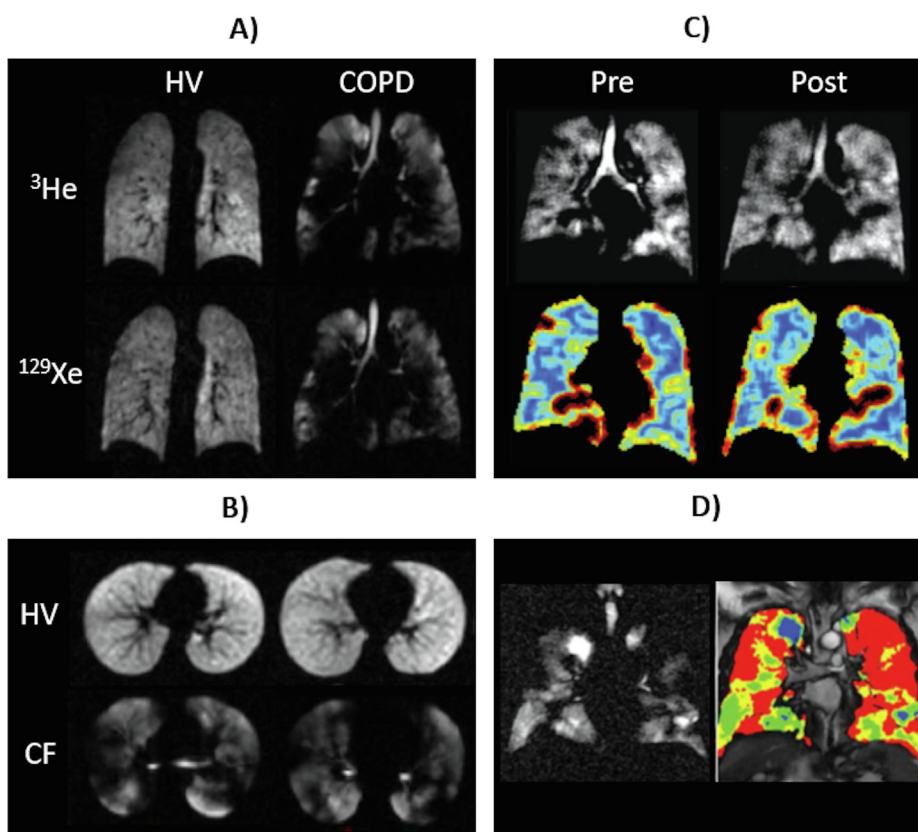
Fig. 2. Ventilation imaging. (a) [3]He and [129]Xe ventilation images of a healthy non-smoker and a patient with COPD, adapted with permission from [157]. (b) [129]Xe ventilation images of a healthy 6-year-old (HV, FEV$_1$ = 95%) and an 11-year-old with CF (CF, FEV$_1$ = 102%), adapted with permission from [165]. (c) [129]Xe ventilation images (top) and coefficient of variation maps (bottom; blue = low COV, red = high COV) of a patient with asthma pre- and post-bronchodilator inhalation, adapted with permission from [163]. (d) [129]Xe ventilation image (left) and binning map (right; red = defect, yellow = low intensity, green = medium intensity, blue = high intensity) from an older patient with asthma (FEV$_1$ = 53%), adapted with permission from [155]. (In this case, ventilation defect percentage (VDP) is defined as the ratio of the number of red pixels to the total number of pixels in the whole lung $\times$ 100).

diffuse an average distance ($\bar{x}$) of ~0.5 mm as defined by the 1D diffusion equation, $\bar{x} = \sqrt{2D_0\Delta}$. The alveoli are the smallest restricting structure of the lungs and have a diameter of ~0.2 mm [180]. Thus, on a time-scale of a few ms, ^{129}Xe atoms can encounter the alveolar walls multiple times, restricting the diffusion and leading to a decrease of MR signal attenuation (S) that is described by:

$$S = S_0 e^{-bD} \qquad (2)$$

where S_0 is the MR signal in the absence of diffusion and the b-value (b) represents the diffusion-weighting applied by magnetic field gradients. In the presence of restricting boundaries, the diffusion coefficient (D) is called "apparent diffusion coefficient" (ADC), and is sensitive to the underlying alveolar dimensions.

The most commonly employed method for hyperpolarised gas diffusion-weighted MRI is a modified Stejskal and Tanner pulsed gradient echo sequence [181] that uses two bipolar trapezoid gradient pulses of equal area after RF pulse excitation. The diffusion time (Δ) is defined as the interval between the middle of the first gradient lobe and the middle of the second. Hyperpolarised gas diffusion-weighted MRI sequences are typically implemented in an interleaved fashion, where acquisition of each line of k-space is repeated for each b-value, by altering the diffusion gradient amplitude, before proceeding to the next line. This ensures that each interleaved scan has the same TE and TR, and that motion artefacts and signal attenuation associated with the depolarisation by RF and T_1 are minimised.

The first *in vivo* human ^{129}Xe diffusion measurements were acquired at 1.5 T in two healthy volunteers [182], where a mean ^{129}Xe ADC of 0.040 cm^2/s was obtained using two b-values of 0 and 10 s/cm^2. In subsequent studies of healthy lungs across different field strengths, similar mean ^{129}Xe ADC values were obtained, ranging from 0.035 to 0.050 cm^2/s [157,159,183–185] (Fig. 3b). Healthy lung ^{129}Xe ADC values are therefore approximately 3–4 times smaller than the free diffusion coefficient of ^{129}Xe in air, and 5–6 times smaller than the respective ^{3}He ADC values (~0.2 cm^2/s) in healthy lungs [186,187], reflecting the inherently lower diffusivity of the ^{129}Xe gas.

In a study demonstrating the clinical feasibility of ^{129}Xe diffusion-weighted MRI [184], ^{129}Xe ADC values obtained in COPD patients with emphysema (0.056 cm^2/s) were significantly elevated in comparison to age-matched healthy controls (0.043 cm^2/s). Other studies in COPD patients have reported global ^{129}Xe ADC values ranging from 0.055 to 0.080 cm^2/s [153,157,159,185,315], demonstrating the sensitivity of ^{129}Xe ADC to emphysematous tissue destruction (shown histologically in Fig. 3a). In these studies, the ^{129}Xe ADC value also significantly correlated with clinical measures of lung function, such as spirometry, the transfer factor of the lung for carbon monoxide (T$_{LCO}$; a measure of gas exchange), and quantitative CT metrics of emphysema.

Further studies have demonstrated that ^{129}Xe ADC is elevated, relative to younger healthy lungs, in older healthy volunteers [184], ex-smokers [157,185,188], and in patients with idiopathic pulmonary fibrosis [189] and lymphangioleiomyomatosis [168].

^{129}Xe ADC measurements are highly repeatable in COPD patients [157], and demonstrate excellent linear correlation with ^{3}He ADC across a range of microstructural length scales [157,159,185,315], indicating that ^{129}Xe ADC mapping is a robust methodology for imaging the lung microstructure. Importantly, ^{129}Xe ADC acquired from explanted human [190] and animal [191,192,316] lungs are significantly correlated with histologically derived mean linear intercept (Lm), a widely accepted measure of airspace size. Whilst the ADC value is sensitive to changes in alveolar dimensions, the measured ADC is also dependent upon
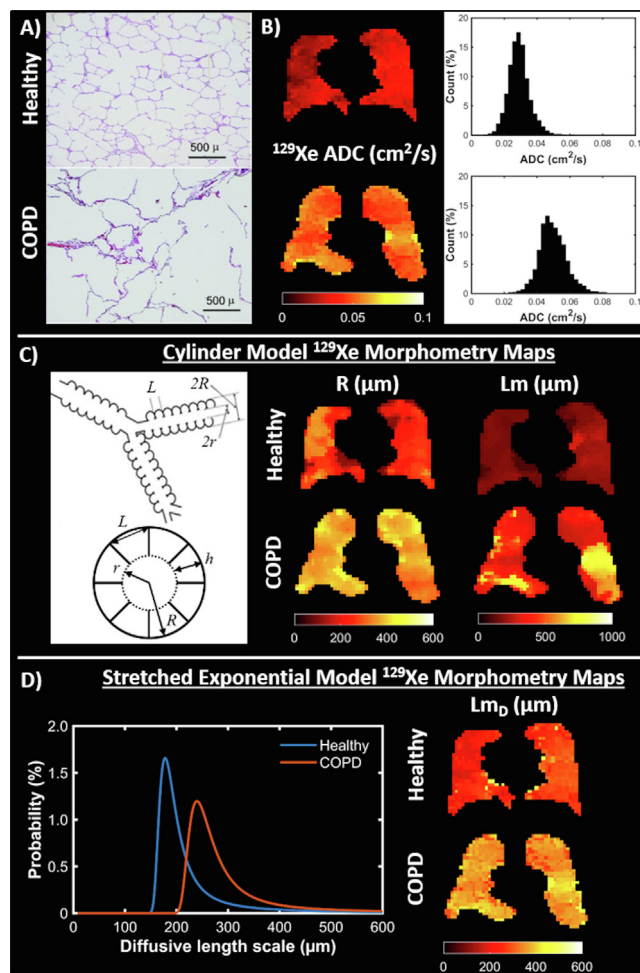

Fig. 3. Diffusion imaging. (a) Examples of histological slides from a healthy lung (top) and COPD lung with emphysema (bottom) that are used to calculate mean linear intercept (Lm) measurements, adapted with permission from [307]. (b) ^{129}Xe ADC maps and whole lung ADC histograms for a healthy volunteer (23-year-old female, top) and COPD patient (68-year-old male, bottom). (c) (Left) Schematic drawing of the cylindrical model of acinar airway geometry based upon the Haefeli-Bleuer and Weibel acinar geometry [212], adapted with permission from [308]. (c) (Right) Cylinder model ^{129}Xe lung morphometry maps of acinar airway radius (R) and mean linear intercept (Lm) in the same healthy volunteer and COPD patient as in (b). (d) (Left) Probability distributions of diffusive length scale derived from the stretched exponential model for the same healthy volunteer and COPD patient. (d) (Right) Stretched exponential model ^{129}Xe lung morphometry maps of mean diffusive length scale (Lm$_D$) for the same healthy volunteer and COPD patient.

experimental acquisition parameters such as B$_0$ field strength [193], and diffusion-encoding pulsed gradient strength, orientation and timing [194–196]. As such, it is difficult to directly link ADC measurements with lung morphometry parameters from histology, and to compare data between different sites that were acquired with different diffusion-weighting sequence parameters.

6.1. Theoretical models of hyperpolarised gas diffusion

The numerous airways of various sizes and orientations with respect to the diffusion-encoding pulsed gradient contained within each diffusion-weighted image voxel manifest as a non-Gaussian diffusion regime with a signal behaviour that deviates from the mono-exponential decay in Eq. (2) [197]. Theoretical models of hyperpolarised gas diffusion have been proposed to account for this non-Gaussian diffusion MR signal behaviour and extract measurements of acinar length scales. Much work has been performed
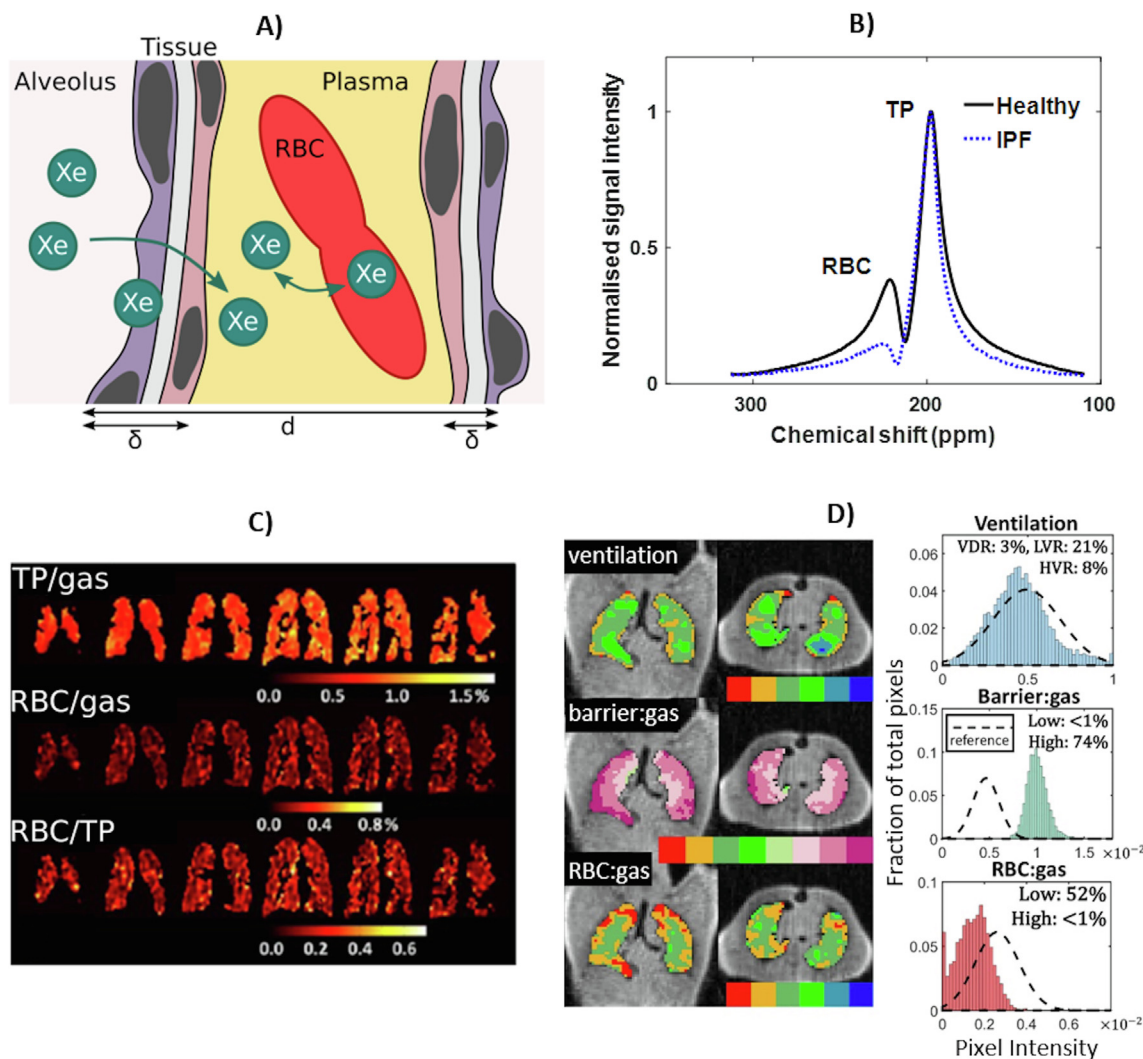
Fig. 4. Probing gas exchange. (a) Cartoon of diffusive exchange of xenon gas from alveolus to capillary, via the parenchymal tissue barrier. The tissue wall thickness (air-blood barrier thickness) is represented by δ, and the total septal wall thickness separating neighbouring alveoli is represented by d. (b) ^{129}Xe MR spectra obtained from a healthy subject (black line) and a patient with IPF (blue line). (c) IDEAL CSI of dissolved ^{129}Xe in the lungs of a patient with moderate COPD, illustrated in the form of ratio maps (reproduced with permission from [104]). (d) Representative binning maps and histograms derived from Dixon-based dissolved-phase ^{129}Xe MRI acquired from a patient with IPF, highlighting the characteristic high TP (barrier) signal and low RBC signal compared with healthy normal subjects (dashed histogram), adapted with permission from [251]. (The notation barrier: gas is equivalent to TP/Gas.)

in modelling the effects of restricted ^{3}He and ^{129}Xe diffusion using geometrical models of lung microstructure that include: cylindrical geometries [198–201], acinar trees [202], branching structures [203–205], alveolar ducts [203], and porous media models [206,207]. Alternative strategies have also been proposed that do not rely on geometrical assumptions of acinar structure: q-space transform analysis [208,209], diffusion kurtosis [210] and stretched exponential models [95,101,211]. To date, cylindrical geometry [201], and stretched exponential [95] models are the only theoretical gas diffusion models that have been used to derive estimates of acinar length scales on a voxel-by-voxel basis from *in vivo* ^{129}Xe diffusion MRI measurements, akin to those from obtained from histology.

The relatively small variation in acinar airway radii across the lungs [212] forms the foundation for a model of acinar airway geometry, known as the "cylinder" model [198,200]. In this model, the acinar airways are modelled as infinitely long cylinders that are covered by alveolar sleeves containing eight alveoli and are characterised by two parameters, the outer acinar airway radii (R), and alveolar sleeve depth (h) (Fig. 3c). Underpinning this acinar airway

geometry is a model of anisotropic diffusion, where more diffusion restriction exists perpendicular to the airway axis due to the alveolar walls, while less restriction is observed along the airway axis [198]. The derived longitudinal (D_L) and transverse (D_T) diffusion coefficients are related to the cylindrical airway geometrical parameters (R and h) by phenomenological expressions derived from Monte-Carlo simulations [199–201]. Additional parameters such as the alveolar volume (V_{Alv}), alveolar surface area (S_{Alv}), and mean chord length (Lm) can then be derived based upon the underlying cylindrical airway geometry.

An alternative theoretical model of hyperpolarised gas diffusion signal behaviour in the lungs is the stretched exponential model, in which *in vivo* estimates of alveolar length scales are derived without making assumptions about the geometry of the lung microstructure [95,101,211]. In this model, the stretched exponential function is fitted to the measured macroscopic voxel signal attenuation that can be represented as a superposition of signals with different apparent diffusivities (D) arising from airways with different sizes and orientations [95]. A probability distribution of apparent diffusivities can be estimated from the stretched expo-

nential function parameters [213] and subsequently related to diffusive length scales, representative of the distribution of microscopic dimensions of the acinar airways (i.e. the diffusion-restricting boundaries) contained within a given voxel. The shape of this distribution is comparable to that of intercept lengths measured by histology, and can be used to derive a mean diffusion length scale (Lm_D) representative of mean acinar airway dimensions within a voxel (Fig. 3d).

The first *in vivo* measurements of ^{129}Xe lung morphometry were measurements of R and Lm derived from the cylindrical model [201] in a healthy subject and a patient with cystic fibrosis [214]. The first patient studies of *in vivo* ^{129}Xe lung morphometry measurements were presented in four healthy never-smokers and four ex-smokers with COPD [215,216]. Cylindrical model anisotropic diffusion coefficients and morphological parameters R and Lm were significantly increased in COPD patients while h was reduced compared with the healthy group. Further patient studies using the stretched exponential model have demonstrated elevated ^{129}Xe Lm_D, with respect to young healthy lungs, in the lungs of ex-smokers, and in patients with IPF and COPD [95,189].

Excellent agreement between ^{129}Xe and ^{3}He lung morphometry measurements derived from the stretched exponential and cylindrical geometry model has been demonstrated across a range of acinar length scales [95]. However, the validation of ^{129}Xe lung morphometry measurements derived from theoretical gas models against gold standard methods for morphometry measurement (namely, histology) has to date been restricted to preclinical studies. For example, ^{129}Xe lung morphometry measurements from the cylindrical geometry model were compared to histology in healthy mice lungs [316], and in rat lungs instilled with disease models of emphysema and radiation-induced lung injury [217–219]. Strong correlations were observed between histologically derived mean linear intercept and cylindrical geometry parameters. Furthermore, good agreement (10–30 μm difference) was observed between ^{129}Xe MR-derived Lm and mean linear intercept from histology [218,316].

In conclusion, diffusion-weighted MR imaging with hyperpolarised ^{129}Xe is a robust methodology that is sensitive to acinar airspace size changes expressed in terms of ADC values and *in vivo* lung morphometry measurements from theoretical gas diffusion models.

7. Probing gas exchange with dissolved-phase ^{129}Xe lung MRI and MRS

The primary function of the lungs is to facilitate the exchange of gases between the alveolar airspace and pulmonary capillaries. However, there is currently a lack of robust, quantitative biomarkers for spatially resolved assessment of pathological gas exchange impairment, and with sensitivity to disease progression and response to treatment. Dissolved-phase ^{129}Xe MRS/I – wherein ^{129}Xe spins dissolved in the lung parenchyma and capillaries are detected during their diffusive exchange with ^{129}Xe gas in the alveoli (Fig. 4a) – may offer a solution.

7.1. Spectroscopic methods

The first *in vivo* HP ^{129}Xe MR lung spectra were acquired from rat and mouse lungs [220,221], and revealed the existence of multiple dissolved-phase ^{129}Xe resonances, distinct from the dominant resonance of gaseous ^{129}Xe in the alveoli. Shortly afterwards, similar resonances were observed in the human pulmonary system [222], and with the aid of *in vitro* studies [108,223], the two *in vivo* dissolved-phase ^{129}Xe resonances – tissue and blood plasma (TP) at ~197 ppm and red blood cells (RBCs) at 216–222 ppm –

were identified. Representative dissolved-phased ^{129}Xe NMR spectra obtained from the lungs of a healthy volunteer and a patient with idiopathic pulmonary fibrosis (IPF) are shown in Fig. 4b.

Several means to quantify pulmonary gas exchange *in vivo* by MR spectroscopy with hyperpolarised ^{129}Xe have been reported. In the chemical shift saturation-recovery (CSSR) experiment, the MR signal of dissolved-phase ^{129}Xe is saturated with a selective 90° RF pulse and the subsequent signal increase due to exchange with alveolar gaseous HP ^{129}Xe is recorded as a function of post-saturation delay by MR spectroscopy. It was first reported in canines that the dissolved-phase ^{129}Xe signal as a function of delay time shows two distinct trends: (i) an initial exponential increase with a plateau at ~200 ms, due to the saturation of parenchymal tissue with fresh HP ^{129}Xe signal (i.e. related to gas exchange); and (ii) an approximately linear increase after ~1 s [224] due to blood flow (i.e. related to perfusion) [225]. Xenon gas exchange can be modelled by considering two adjacent alveoli separated by a "slab" of parenchymal tissue and capillaries (see Fig. 4a) in order to derive metrics of pulmonary function, including alveolar surface area to volume ratio (S/V), parenchymal septal thickness and capillary blood flow [225–229]. The CSSR method has been applied to assess gas exchange impairment in small animal emphysema and human patients with COPD, revealing tissue destruction (reduced S/V) [230,231] and alveolar septal wall thickening [188,232]. In IPF patients, pronounced septal thickening has been observed, consistent with pulmonary fibrosis [106,227]. Model-derived lung function metrics are sensitive to the lung inflation level [231,232,317], and the septal thickness correlates with the clinical standard pulmonary function test for gas exchange (T_{LCO}) [106,232] and was found to be repeatable in patients with COPD [231].

Steady-state spectroscopic measurements (i.e. acquired with a single delay time) also allow quantitative assessment of gas exchange. The ratio of the ^{129}Xe resonances of RBC to TP in the lung is sensitive to thickening of the alveolar septae in IPF (Fig. 4b) and also correlates with T_{LCO} [233]. This approach exhibits longitudinal sensitivity to disease progression in IPF where T_{LCO} showed no change [234], which has implications for disease management. Recent efforts have been concentrated on characterisation of the dissolved-phase ^{129}Xe resonance lineshapes [235], accurate chemical shift referencing [236] and investigating oscillations in the RBC signal (and chemical shift) which track the cardiac cycle [237,238]; the latter is discussed further in Section 8.

7.2. Imaging methods

As pathological gas-exchange impairment is spatially heterogeneous, 3D spatial information is required for improved disease management and targeted treatment in diseases such as IPF. Simultaneous imaging of dissolved-phase and gaseous-phase ^{129}Xe in the lung within a single read-out can be achieved by tuning to the dissolved ^{129}Xe resonance and choosing a low imaging bandwidth to exploit the chemical shift "artefact" [109]. However, this approach is constrained by SNR and resolution, and use of an ultra-short echo time radial sequence with interleaved frequency switching between dissolved-phase and gaseous-phase ^{129}Xe offers improved SNR performance in light of the short T_2^* [239,240]. While these techniques enable imaging of dissolved phase ^{129}Xe (TP and RBC), distinction of the two dissolved-phase ^{129}Xe compartments is important for quantitative gas exchange measurements. Free induction decay (FID)-based chemical shift imaging (CSI) with Cartesian phase encoding allows the acquisition of spatially-resolved spectra [241], though it suffers in terms of speed and spatial resolution. Dixon-type acquisitions [242] can be used to separate the TP and RBC resonances by exploiting the

phase difference between them. In particular, single-point Dixon imaging has been developed for ^{129}Xe gas exchange imaging; radially-encoded images are acquired at a TE where the phase difference between TP and RBC resonances is 90° [243]. The resulting RBC image represents ^{129}Xe that has fully traversed the lung tissue barrier. Compared with "multi-point" approaches, the single-point method suffers from contamination of dissolved-phase ^{129}Xe images with gas-phase ^{129}Xe signals, though a technique for removal of this contamination has been reported [244]. An alternative approach is based on iterative decomposition with echo asymmetric and least-squares estimation (IDEAL) [245], which involves acquisition of images at multiple echo times to improve the separation of gaseous, TP- and RBC-dissolved ^{129}Xe [104]. Both radial [104,318] and spiral [246,247] read-outs have been reported. The single-point Dixon method is sensitive to regional gas-exchange impairment in IPF, and dissolved-phase ^{129}Xe MRI biomarkers show agreement with T_{LCO} [248,318]. Recent data demonstrate the sensitivity of dissolved-phase ^{129}Xe MRI to IPF disease progression [249], and distinct gas-exchange features in asthmatics and COPD patients [104,232] and a range of cardiopulmonary pathologies [250].

While IDEAL or Dixon images are typically presented as ratio maps of RBC/TP, RBC/Gas or TP/Gas signals (see Fig. 4c), recent efforts have been focussed on improving quantitative analysis techniques, such as binning to create graded colour signal ratio maps to facilitate clinical interpretation [248,251] (see Fig. 4d). In addition, further exploration of the reproducibility of these techniques is likely to aid clinical dissemination [252,253]. Recent reports demonstrating the regional assessment of CSSR-type gas-exchange dynamics [254,255], and novel techniques for imaging the cardiogenic oscillations of the ^{129}Xe RBC resonance [256], may pave the way to maximising the obtainable functional information about pulmonary gas exchange with hyperpolarised ^{129}Xe.

As *direct* dissolved-phase ^{129}Xe imaging techniques are hampered by low SNR and short T_2^*, SNR benefits may be obtained by *indirect* gas exchange imaging, i.e. by detection of gaseous-phase ^{129}Xe. The xenon polarisation transfer contrast (XTC) method is one such indirect technique, and involves (i) gradient echo imaging of gaseous phase ^{129}Xe; (ii) a series of inversion/saturation RF pulses centred on the dissolved ^{129}Xe resonances (to weight the signal intensity according to gas exchange); and (iii) further acquisition of gaseous-phase ^{129}Xe images [257,258]. The regional gas depolarisation between the two images is related to the gas exchange, can be modelled in terms of lung tissue density and thickness [258], and correlates with histological measurements of alveolar septal volume [259]. Repeating the XTC acquisition at several inter-pulse delay times (multiple exchange time XTC (MXTC) [260,261]) permits mapping of a characteristic gas exchange constant and has been applied to quantify tissue loss in COPD [261]. The main limitation of XTC is that the TP and RBC resonances cannot be separated, since their close chemical shift and rapid chemical exchange inhibit selective inversion.

8. ^{129}Xe dissolved in human blood

8.1. ^{129}Xe relaxation in human blood

The ^{129}Xe relaxation rate in blood has been studied in previous NMR experiments performed by several groups. In work conducted at a field strength of 4.7 T with hyperpolarised ^{129}Xe [111], the spin–lattice relaxation time, $T_1(^{129}$Xe$)$, in red blood cells (RBC) within whole blood was found to increase with blood oxygenation (sO_2), with $T_1(^{129}$Xe$)$ values of 4 s and 13 s in deoxygenated and oxygenated blood, respectively. The same group also performed measurements with thermally polarised ^{129}Xe samples and found the RBC $T_1(^{129}$Xe$)$ in deoxygenated and oxygenated blood samples

to be lower; 2.7 ± 0.22 s and 7.88 ± 0.16 s [262]. Work at a field strength of 1.5 T [223], also reported an increase in $T_1(^{129}$Xe$)$ with blood oxygenation (2.88 ± 0.27 s deoxygenated and 5.71 ± 0.35 s oxygenated blood), and found the R_1 = 1/ T_1 to increase (or $T_1(^{129}$Xe$)$ to decrease) non-linearly with blood oxygenation – see Fig. 5b. Both groups found the $T_1(^{129}$Xe$)$ to be highest in blood that had been equilibrated with carbon monoxide, which locks the haemoglobin molecule into a conformation similar to fully oxygenated haemoglobin; Albert et al. [262] reported a value $T_1(^{129}$Xe$)$ = 11 ± 2 s and Tseng et al. [223] reported a value $T_1(^{129}$Xe$)$ = 7.84 ± 0.47 s.

In contrast, in a study conducted with a foam preparation of blood, at a field strength of 4.7 T [263], the opposite dependence of $T_1(^{129}$Xe$)$ on blood oxygenation was observed. The $T_1(^{129}$Xe$)$ was reported to decrease from 40 s in deoxygenated blood to 20 s in oxygenated blood, and it was deduced that interactions between xenon and paramagnetic bubbles of oxygen gas in the blood were the principal cause of spin-lattice relaxation. The interior of the bubbles provides a residency space for gaseous xenon and oxygen, and the bubble-walls provide a surface compartment for the oxygen-exposed gaseous xenon in which to dissolve. Xenon gas and paramagnetic oxygen gas in the bubbles (undergoing nuclear-electron dipole-dipole $T_1(^{129}$Xe$)$ relaxation with a dependence inversely proportional to pO_2) can readily exchange with the dissolved xenon in this regime and as such, the effect of oxygen on $T_1(^{129}$Xe$)$ may have been overestimated.

Recently, RBC $T_1(^{129}$Xe$)$ was examined over the widest yet range of blood oxygenations (sO_2 values of 0.06–1.00) using hyperpolarised ^{129}Xe [113] at a field strength of 1.5 T, where it was found that T_1 increases non-linearly with blood oxygenation [see Fig. 5b], in agreement with the previous findings of Ref. [223]. In addition, the authors in Ref. [113] developed a two-site (RBCs and plasma) exchange model of the magnetization dynamics of ^{129}Xe in whole blood samples to determine 10 constants that underpin and describe ^{129}Xe NMR relaxation and exchange in isolated RBCs and isolated plasma, as well as in whole blood samples. Four constants were extrapolated by fitting the equation $1/T_1 = \kappa \left[1 - \exp\left(r_{sO_2} sO_2\right) \right] + 1/T_1^{dHb}$ to the blue circle data in Fig. 5b. Here $\kappa = 4.6 \times 10^{-6}$ s^{-1} is a scaling constant, r_{sO_2} = 11.1, is a "relaxivity index" characterizing the rate of change of ^{129}Xe relaxation as a function of blood oxygenation and $1/T_1^{oHb}$ = 0.13 s^{-1} and $1/T_1^{dHb}$ = 0.42 s^{-1} are the ^{129}Xe relaxation rates in fully oxygenated blood and fully deoxygenated blood, respectively. Two rate constants, k_a = 0.022 ms^{-1} and k_b = 0.062 ms^{-1}, were determined for xenon diffusing between RBCs and plasma, respectively and two constants describing ^{129}Xe relaxation within isolated plasma samples were determined: r_{sO_2} = 0.075 s^{-1} mM^{-1} is the relaxivity index of ^{129}Xe in the presence of dissolved molecular O_2 within plasma and $1/T_{1,b}^0$ = 0.046 s^{-1} is the ^{129}Xe relaxation rate in the absence of dissolved O_2. The final two constants determined from the model represent the intrinsic ^{129}Xe-RBC relaxation rates, $1/T_{1,a}^{oHb}$ = 0.19 s^{-1} and $1/T_{1,a}^{dHb}$ = 0.84 s^{-1}, in oxygenated blood and deoxygenated blood, respectively.

Knowledge of these constants is important for future experiments involving modelling of the signal dynamics of ^{129}Xe as it travels in the blood from lungs to distal tissues such as the brain and kidneys.

8.2. ^{129}Xe chemical shift in human blood

Studies at a field strength of 1.5 T have shown that the ^{129}Xe chemical shift in RBCs within whole blood increases non-linearly with RBC blood oxygenation [237,264] (see Fig. 5c and d) in a similar manner to the ^{129}Xe relaxation dependence on blood oxygenation discussed above. The ^{129}Xe chemical shift in plasma remains
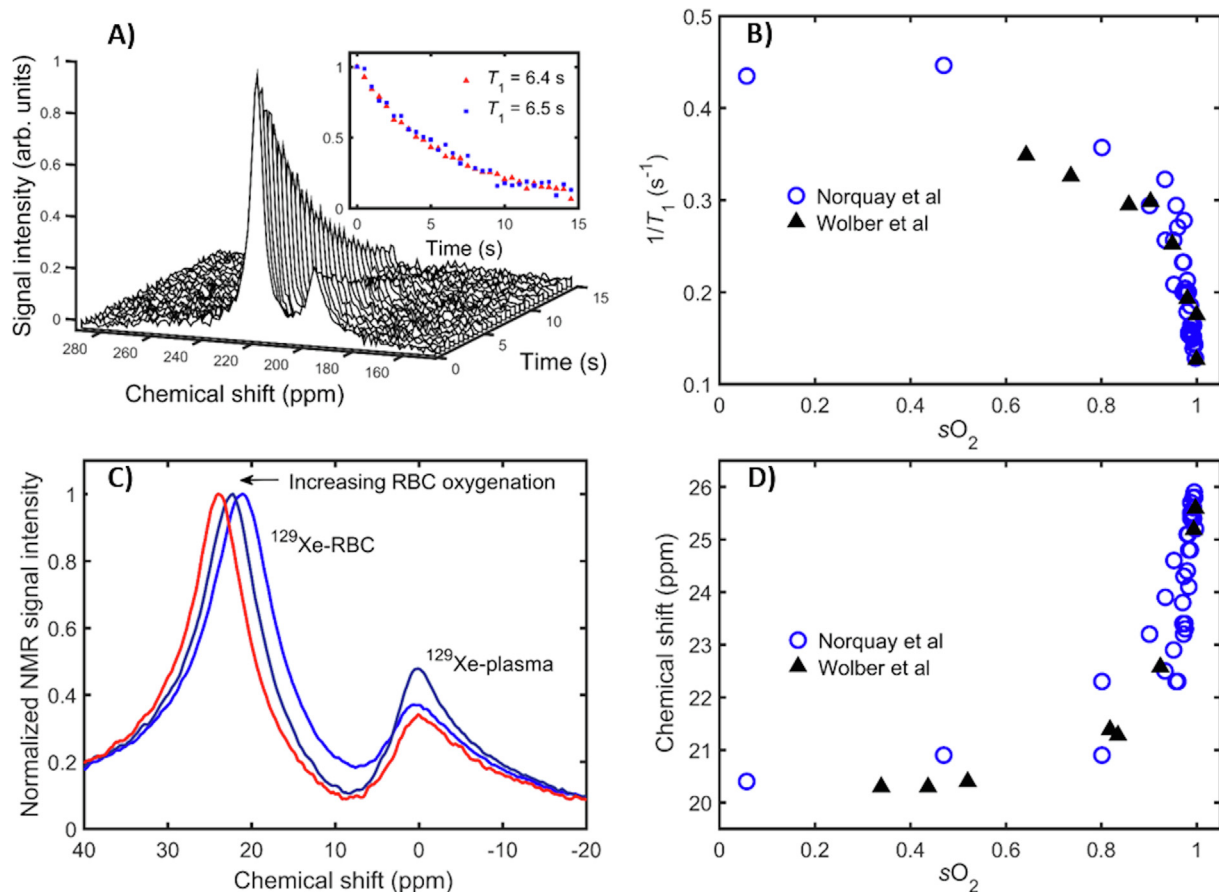
Fig. 5. ^{129}Xe dissolved in human blood. (a) Decaying spectra from ^{129}Xe dissolved in blood acquired with inter-pulse delay = 0.5 s. The inset shows a fit performed on the decreasing ^{129}Xe NMR signal (integrals of ^{129}Xe-red-blood-cell (RBC) and ^{129}Xe-plasma absorption peaks) in order to establish ^{129}Xe-RBC (red triangles) and ^{129}Xe-plasma T_1 values (blue squares). Here 0 ppm refers to the ^{129}Xe gas-phase resonance frequency. The decaying spectra are from a blood sample with sO_2 = 0.98. The data in (b) are the measured ^{129}Xe relaxation rates ($1/T_1$) in RBCs as a function of RBC oxygenation from [237] (open blue circles) and [264] (solid black triangles). In (c) it can be seen that with increasing oxygenation, the peak associated with ^{129}Xe dissolved in RBCs is seen to shift measurably towards higher resonance frequency. Here 0 ppm is in reference to the ^{129}Xe-plasma resonance frequency. Shown in (d) is a plot of the change in ^{129}Xe-RBC chemical shift as a function of RBC oxygenation from Refs. [237] (open blue circles) and [264] (solid black triangles).

fixed in frequency over the whole blood oxygenation range (see Fig. 5c). Using the ^{129}Xe-plasma resonance as a 0 ppm reference, the ^{129}Xe-RBC chemical shift was observed to increase from 20.5 ppm in fully deoxygenated blood to 26 ppm in fully oxygenated blood (Fig. 5d). This observed chemical shift vs. oxygenation behaviour is consistent when the same experiment is performed at magnetic field strengths of 1.5 T and 3 T [237], indicating that it is a field-strength-independent effect.

Knowledge of tissue oxygenation can provide insight into the pathophysiology of a variety of diseases, e.g. in the discrimination of the penumbra following stroke [265] and identification of ischemia following myocardial infarction [266]. In lung diseases such as asthma and COPD, hypoxia can influence the lifetime and the functionality of neutrophils that are associated with inflammation in the lungs [267]. The demonstrated sensitivity of the ^{129}Xe-RBC chemical shift to blood oxygenation [237,264] is promising as it could be used to non-invasively probe tissue oxygenation within the lungs and well-perfused tissues distal to the lungs. ^{129}Xe-RBC resonance shifts with lung oxygenation have been reported *in vivo* in healthy volunteers during breath hold [268], and in patients with IPF [233] where a decrease in the ^{129}Xe-RBC resonance frequency (indicating lower oxygenation) was observed.

Norquay et al. [237] used the *in vitro* data of the ^{129}Xe-RBC chemical shift dependence on sO_2 (Fig. 5d) as a calibration curve to determine absolute oxygenation changes in the alveolar capillary bed during a breath-hold challenge undertaken by healthy volunteers.

For a TR of 800 ms (of the order of the RBC alveolar capillary transit time), it was observed that the ^{129}Xe-RBC chemical shift exhibited a periodic modulation at the same frequency as the ^{129}Xe-RBC signal oscillation, and with a 180° phase difference. Using the *in vitro* calibration data, the sO_2 in two healthy volunteers at the start of the breath-hold was measured to be ~0.87, dropping to ~0.80 after 35 s of breath-hold apnea. The experiment was repeated for a shorter TR of 100 ms, where both the ^{129}Xe-RBC and ^{129}Xe-TP signals were observed to oscillate close to the cardiac pulsation frequency, in agreement with ^{129}Xe-RBC and ^{129}Xe-TP signal oscillations observed in Refs. [269 and 270]. (Lower frequency oscillations observed at TR = 800 ms are likely an alias of the higher frequency oscillation observed for TR = 100 ms.) It was concluded that the observed signal and chemical shift oscillations could be attributed to changes in blood flux/oxygenation in the capillaries during the cardiac cycle. These ^{129}Xe-RBC cardiogenic oscillations have recently been observed in patients with COPD, IPF, left heart failure (LHF), and pulmonary arterial hypertension (PAH) [238,250]. It was found that IPF patients exhibited increased RBC amplitude and shift oscillations compared to healthy volunteers. Patients with COPD and PAH both exhibited decreased RBC amplitude oscillations compared to healthy volunteers, and interestingly LHF was distinguishable from PAH by enhanced RBC amplitude oscillations. Thus, ^{129}Xe-RBC cardiogenic oscillation measurements hold promise for the distinction of functional characteristics of different cardiopulmonary diseases.

9. Imaging inhaled hyperpolarised [129]Xe beyond the lungs

The blood supply for the brain, kidney, skeletal muscle, liver and gastrointestinal system accounts for 80% of the cardiac output [271]. Among these distal organs, the brain and kidney have short arterial delivery times of ~4 s [272] and ~2 s respectively from the lungs, short enough for inhaled HP [129]Xe to retain polarisation until delivery, enabling direct MR imaging [60,63,273,274].

[129]Xe dissolved in the head *in vivo* exhibits five distinct NMR spectral peaks corresponding to: grey matter (196 ppm), white matter (193 ppm), interstitial and cerebrospinal fluids (200 ppm), soft muscular tissue (188 ppm) and red-blood cells (216 ppm) [11,62,63,114,275,276], as seen in Fig. 6a. The NMR spectral peak from [129]Xe dissolved in the grey matter dominates the spectrum [62,114]. With a cerebral blood flow for grey matter of 65 mL per minute per 100 g of tissue [277], cerebral blood volume of 5 mL per 100 g of tissue [277] and Ostwald's grey matter to blood partition coefficient of 0.88 [278] in healthy normal individuals, the inhaled HP [129]Xe dissolved in the cerebral blood rapidly infuses in to the grey matter tissue reaching a concentration that enables direct MR imaging over a breath-hold of 24 s [60]. The MR image that is obtained (Fig. 6b) is a map of uptake of inhaled gas into the brain tissue across the intact blood-brain barrier, which is indicative of underlying physiology such as the regional cerebral blood flow and volume, regional mean transit time and gas transfer rate across the blood-brain barrier [60,319]. Pre-clinical studies in rat brains have demonstrated image contrast sensitive to sensory

stimuli [279] and induced ischemia [280]. Recently, there has been growing interest in the potential clinical sensitivity of inhaled HP [129]Xe to human brain pathology such as Alzheimer's disease [273] and stroke [281], as shown in Fig. 6c. HP [129]Xe brain MRI benefits from the fact that inhaled [129]Xe is safe and non-invasive, and crosses the intact blood-brain barrier, when compared to routine clinical CT and MR imaging techniques which use injected iodine- and gadolinium-based contrast agents respectively, both of which lead to a concern for patient safety [282–284]. In contrast to arterial spin labelling ^{1}H MR imaging, HP [129]Xe brain MRI does not require averaging [285], has no undesired signal from the intra-vascular compartment [60] and the image contrast directly depends on the underlying physiology.

In the kidneys, up to 3 spectral peaks have been demonstrated *in vivo*, two of which have been assigned to red blood cells (217 ppm) and tissue (and plasma) (198 ppm), while the origin of the third peak at 192 ppm is yet to be determined [274,276,286,287]. A fourth peak at ~188 ppm is believed to originate from fat tissue in the lower abdomen, outside of the kidneys. With renal perfusion of 170 to 220 mL per minute per 100 mL of tissue [288,289], the HP [129]Xe saturates in the extra-vascular kidney compartment more quickly than in the brain, although with much lower spin density due to more rapid clearance of blood from the kidney. Nevertheless, imaging HP [129]Xe dissolved in the kidney benefits from shorter arterial transit time, thereby less loss of polarisation due to T_1 decay in blood prior to delivery, and a fast time-resolved acquisition can be used to characterise signal
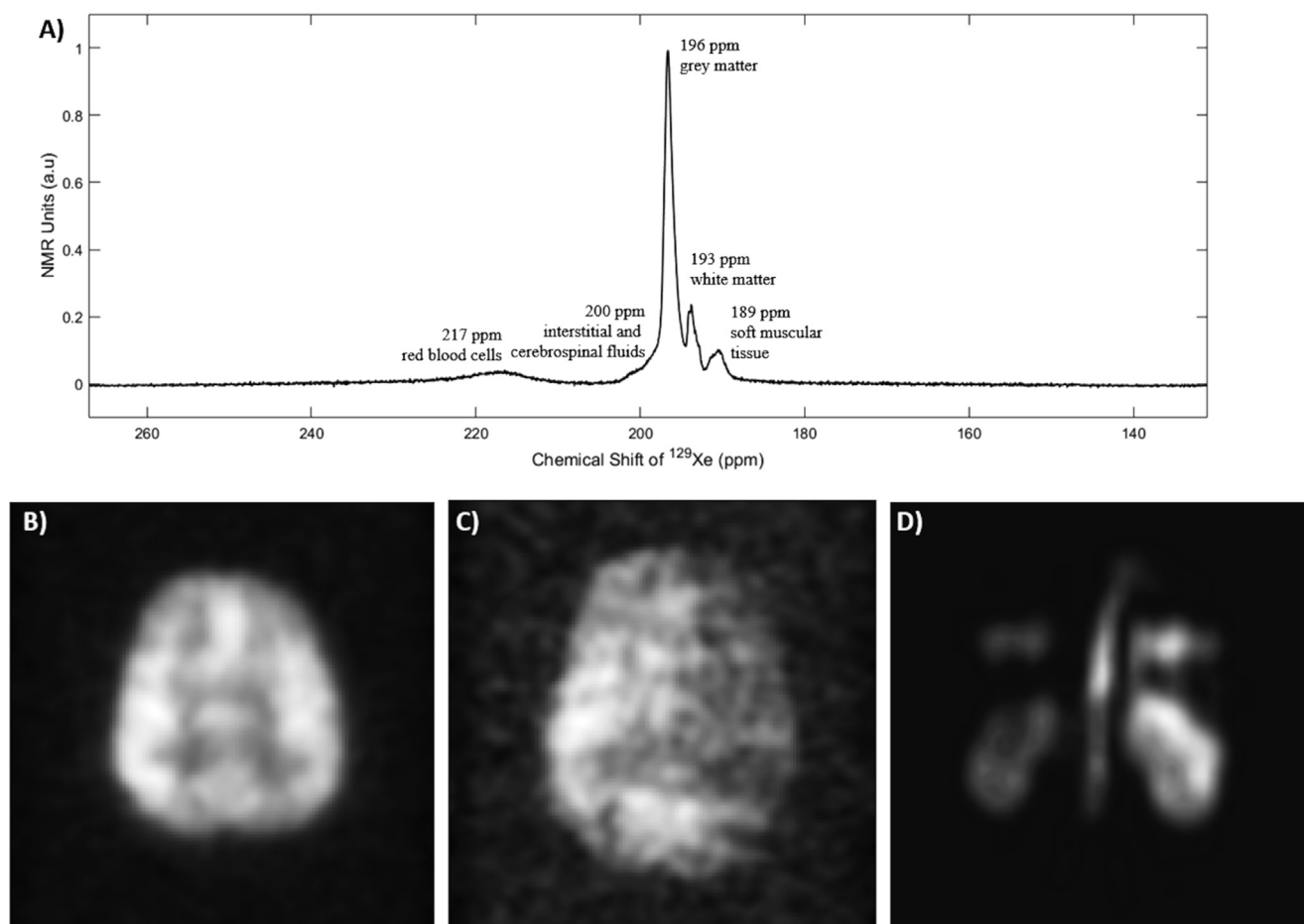
Fig. 6. [129]Xe beyond the lungs. (a) Spectrum of HP [129]Xe dissolved in the human head. Spectral peaks: 189 ppm: soft muscular tissue, 193 ppm: white matter, 196 ppm: grey matter, 200 ppm: interstitial and cerebrospinal fluids, and 217 ppm red blood cells. Brain perfusion images of (b) a healthy volunteer (adapted with permission from [60]) and (c) a volunteer with established stroke (adapted with permission from [281]), using inhaled hyperpolarised [129]Xe. (d) Kidney perfusion images of a healthy volunteer using inhaled hyperpolarized [129]Xe, adapted with permission from [63].

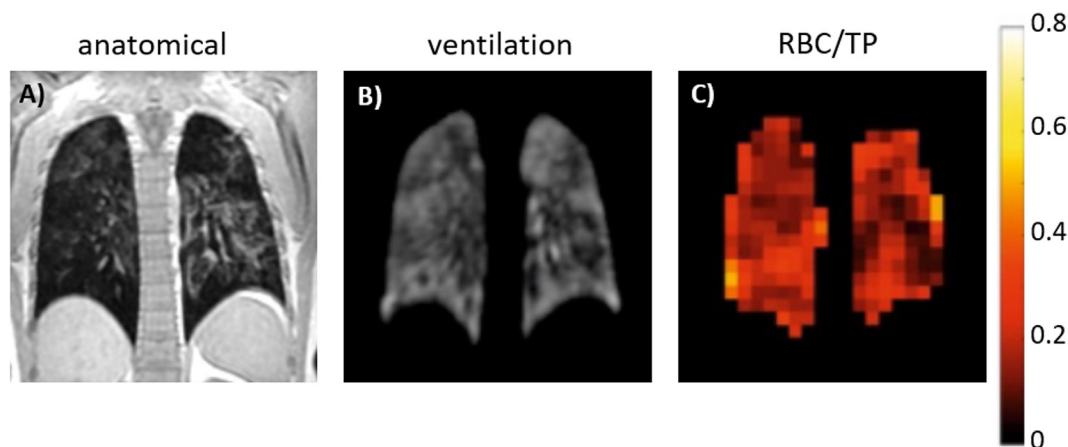**Fig. 7.** [129]Xe MRI in acute COVID-19. (a) ^{1}H anatomical SPGR image, (b) [129]Xe ventilation image and (c) [129]Xe RBC/TP map acquired with an IDEAL sequence [318] of a coronal mid-posterior slice in a patient with acute COVID-19. For this slice, ventilated volume percentage = 99.6% and RBC/TP = 0.188 (mean RBC/TP in healthy volunteers = 0.47 [318]). RBC/TP = red blood cells to tissue and blood plasma ratio.

dynamics [286,287]. Recent studies demonstrating MR spectroscopy and imaging of human kidneys *in vivo* using inhaled HP [129]Xe [274,286,287] are encouraging, as shown in Fig. 6d.

10. Conclusions and future perspectives

[129]Xe lung MR is a versatile tool for the examination of lung function and structure, providing quantitative physiological information. Ventilation and diffusion MRI are well-established, repeatable techniques that are sensitive to early-stage lung disease [157,167–169,185,188]. They have the potential to detect lung abnormalities earlier than spirometry [168,169] and structural imaging [167,290], allowing early intervention/therapy to mitigate further damage. Moreover, the sensitivity of [129]Xe ventilation imaging to therapy response [158,163,171,172] coupled with its high repeatability should enable clinical trials of novel therapeutics with small patient numbers, as has been demonstrated with [3]He ventilation MRI [291,292]. Crucially, the lack of ionising radiation associated with [129]Xe MR is important when considering repeated imaging, and allows safe longitudinal monitoring of disease progression and studies of therapeutic response. This and the functional sensitivity of [129]Xe MRI are real advantages in comparison to CT, the clinical gold standard for lung imaging. Nevertheless, the complementary use of [129]Xe MRI alongside CT and/or advanced ^{1}H morphological MRI allows the investigation of structure-function relationships to gain insights into disease pathology [167,168,293,294].

Dissolved-phase [129]Xe MRS/I of the lung is still at an earlier stage of technological development, yet shows great promise as a probe for gas exchange. Increased signal from parenchymal lung tissue and reduced RBC signal indicate interstitial alveolar wall thickening and impaired gas transfer efficiency, and dissolved-phase [129]Xe techniques have demonstrated the sensitivity to distinguish healthy smokers from never-smokers [188] and to detect longitudinal disease progression in patients with IPF earlier than currently used clinical metrics [234,249]. During the course of the current COVID-19 pandemic, evidence is emerging that dissolved-phase [129]Xe lung MRI is sensitive to gas exchange abnormalities in patients with COVID-19 [320]. The first published [129]Xe MRI study in COVID-19 patients [320], conducted after patients had been discharged from hospital, found reduced gas-blood exchange function and lung ventilation with normal alveolar dimensions, while CT images showed substantial recovery compared to the peak stage of COVID-19. Two patients scanned in the acute, symptomatic phase of COVID-19 at the University of

Sheffield showed massively impaired gas exchange despite relatively normal ventilation (Fig. 7), and initial results from a collaboration between Oxford and Sheffield Universities indicate that gas exchange impairment is detectable using [129]Xe MRI in patients three months after being ill with COVID-19 (bbc.co.uk/news/health-55017301). Taken together, these initial findings suggest that dissolved-phase [129]Xe lung MRI may provide a valuable tool for the investigation of COVID-19 lung disease. The concept of a single 3D gas- and dissolved- phase [129]Xe MRI acquisition for regional assessment of gas exchange impairment and ventilation is attractive [192,250,295–297], although currently the gas-phase images obtained from multi-resonant imaging and dedicated ventilation images acquired separately are not interchangeable [297]. Further development of time-efficient, repeatable gas- and dissolved-phase imaging strategies with improved SNR may permit this in the future. In addition, the emergence of dissolved-phase [129]Xe spectroscopy as a means to investigate blood oxygenation *in vivo* [233,237,264] and detect modulations of [129]Xe RBC signal and chemical shift caused by the cardiac cycle [237,270] that differ between patients with different cardiopulmonary disease types [238,250] is of great clinical interest. Furthermore, evidence of reduced gas uptake following stroke [281] and retention of inhaled [129]Xe in the brain in Alzheimer's disease [273] measured by dissolved-phase [129]Xe brain MRI are attractive to the neuroimaging community. It is likely that the multi-faceted potential of dissolved-phase [129]Xe to probe oxygenation and gas exchange processes in the lungs, as well as perfusion in the brain and kidneys, will drive innovation in the field of hyperpolarised [129]Xe MR in the years to come.

With current polarisation technologies, dedicated RF coil design and MR pulse sequence optimisation, high quality data acquisition with progressively lower doses of enriched xenon (86% [129]Xe) and even natural abundance xenon (26% [129]Xe) [78] has been made feasible, paving the way towards low cost [129]Xe MRI. Following UK Medicine and Healthcare Regulatory Authority approval, routine clinical lung imaging has been performed in Sheffield, UK since 2015 [15], a service that has switched almost entirely to [129]Xe in recent years [298]. This important milestone establishes routine clinical [129]Xe lung MRI, opening the door to large-scale clinical evaluation of these methods in patient populations. In parallel, phase III clinical trials are currently in progress in the U.S. to obtain Food and Drug Administration approval for hyperpolarised [129]Xe as a drug-device imaging agent [299], which should help drive international clinical trials.

There is a drive towards standardisation of ^{129}Xe MR acquisition and analysis, to enable multi-site studies of ventilation imaging in the first instance (cpir.cchmc.org/XeMRICTC). A thermally polarised xenon torso phantom for quality assurance has been developed and tested at eight sites across North America [299]. Different approaches to image segmentation for ventilated volumes have been compared [152,154], and substantial inter-reader agreement reported between blinded radiologists [164]. A recent retrospective study of ventilation images acquired at two institutions in children with CF found similar ventilation metrics between sites and strong agreement between two analysts, concluding that multi-centre trials in CF appear to be feasible [166]. Yet, there remains work to be done to standardise image acquisition and analysis between centres, each of which currently has its own established workflow tuned to their situation and preferences. This is critical not only for ventilation imaging, which is most well-developed and closest to clinical translation of the ^{129}Xe MRI techniques, but also for diffusion-weighted ^{129}Xe MRI and up-and-coming techniques such as dissolved-phase ^{129}Xe MRS/I, to facilitate multi-site trials and aid their eventual transition to the clinic.

Declaration of Competing Interest

The authors declare that they have no known competing financial interests or personal relationships that could have appeared to influence the work reported in this paper.

Acknowledgements

References

[1] W. Ramsay, Nobel Lecture – The Rare Gases of the Atmosphere, in: Nobel Media AB, 1904.

[2] D. Raftery, Xenon NMR Spectroscopy, in: G.A. Webb (Ed.), Annual Reports on NMR Spectroscopy, Elsevier, 2006, pp. 205–270.

[3] J. Fraissard, T. Ito, Xe-129 Nmr-study of adsorbed xenon – a new method for studying zeolites and metal-zeolites, Zeolites 8 (1988) 350–361.

[4] A. Kastler, Quelques suggestions concernant la production optique et la détection optique d'une inégalité de population des niveaux de quantification spatiale des atomes. Application à l'expérience de Stern et Gerlach et à la résonance magnétique, J. Phys. Radium 11 (1950) 255–265.

[5] M.A. Bouchiat, T.R. Carver, C.M. Varnum, Nuclear polarization in He-3 gas induced by optical pumping and dipolar exchange, Phys. Rev. Lett. 5 (1960) 373–375.

[6] B.C. Grover, Noble-gas NMR detection through noble-gas-rubidium hyperfine contact interaction, Phys. Rev. Lett. 40 (1978) 391–392.

[7] W. Happer, E. Miron, S. Schaefer, D. Schreiber, W.A. Vanwijngaarden, X. Zeng, Polarization of the nuclear spins of noble-gas atoms by spin exchange with optically pumped alkali-metal atoms, Phys. Rev. A 29 (1984) 3092–3110.

[8] T.G. Walker, W. Happer, Spin-exchange optical pumping of noble-gas nuclei, Rev. Mod. Phys. 69 (1997) 629–642.

[9] D. Raftery, H. Long, T. Meersmann, P.J. Grandinetti, L. Reven, A. Pines, High-field Nmr of adsorbed xenon polarized by laser pumping, Phys. Rev. Lett. 66 (1991) 584–587.

[10] M.S. Albert, G.D. Cates, B. Driehuys, W. Happer, B. Saam, C.S. Springer Jr., A. Wishnia, Biological magnetic resonance imaging using laser-polarized 129Xe, Nature 370 (1994) 199–201.

[11] J.P. Mugler III, B. Driehuys, J.R. Brookeman, G.D. Cates, S.S. Berr, R.G. Bryant, T.M. Daniel, E.E. De Lange, J.H. Downs Iii, C.J. Erickson, W. Happer, D.P. Hinton, N.F. Kassel, T. Maier, C.D. Phillips, B.T. Saam, K.L. Sauer, M.E. Wagshul, MR imaging and spectroscopy using hyperpolarized 129Xe gas: preliminary human results, Magnetic Reson. Med. 37 (1997) 809–815.

[12] M.S. Albert, D. Balamore, Development of hyperpolarized noble gas MRI, Nucl. Instrum. Methods Phys. Res. A 402 (1998) 441–453.

[13] M. Ebert, T. Grossmann, W. Heil, W.E. Otten, R. Surkau, M. Leduc, P. Bachert, M.V. Knopp, L.R. Schad, M. Thelen, Nuclear magnetic resonance imaging with hyperpolarised helium-3, Lancet 347 (1996) 1297–1299.

[14] J.R. MacFall, H.C. Charles, R.D. Black, H. Middleton, J.C. Swartz, B. Saam, B. Driehuys, C. Erickson, W. Happer, G.D. Cates, G.A. Johnson, C.E. Ravin, Human lung air spaces: potential for MR imaging with hyperpolarized He-3, Radiology 200 (1996) 553–558.

[15] J.M. Wild, L. Smith, F.C. Horn, G.J. Collier, A. Swift, N.J. Stewart, M. Rao, G. Norquay, D. Hughes, K. Ugonna, H. Marshall, Hyperpolarised gas MR lung imaing – breaks through to clinical practice, Eur. Respiratory J. 46 (2015) OA4992.

[16] L. Cander, Solubility of inert gases in human lung tissue, J. Appl. Physiol. 14 (1959) 538–540.

[17] J. Hawkins, C. Shilling, Helium solubility in blood at increased pressures, J. Biol. Chem. 113 (1936) 649–653.

[18] P.K. Weathersby, L.D. Homer, Solubility of inert gases in biological fluids and tissues: a review, Undersea Biomed. Res. 7 (1980) 277–296.

[19] J. Ladefoged, A.M. Andersen, Solubility of Xenon-133 at 37°C in water, saline, olive oil, liquid paraffin, solutions of albumin, and blood, Phys. Med. Biol. 12 (1967) 353–358.

[20] N.P. Franks, R. Dickinson, S.L.M. de Sousa, A.C. Hall, W.R. Lieb, How does xenon produce anaesthesia?, Nature 396 (1998), 324–324.

[21] B. Driehuys, S. Martinez-Jimenez, Z.I. Cleveland, G.M. Metz, D.M. Beaver, J.C. Nouls, S.S. Kaushik, R. Firszt, C. Willis, K.T. Kelly, J. Wolber, M. Kraft, H.P. McAdams, Chronic obstructive pulmonary disease: safety and tolerability of hyperpolarized 129Xe MR imaging in healthy volunteers and patients, Radiology 262 (2012) 279–289.

[22] Y. Shukla, A. Wheatley, M. Kirby, S. Svenningsen, A. Farag, G.E. Santyr, N.A. Paterson, D.G. McCormack, G. Parraga, Hyperpolarized 129Xe magnetic resonance imaging: tolerability in healthy volunteers and subjects with pulmonary disease, Acad. Radiol. 19 (2012) 941–951.

[23] L.L. Walkup, R.P. Thomen, T.G. Akinyi, E. Watters, K. Ruppert, J.P. Clancy, J.C. Woods, Z.I. Cleveland, Feasibility, tolerability and safety of pediatric hyperpolarized (129)Xe magnetic resonance imaging in healthy volunteers and children with cystic fibrosis, Pediatr. Radiol. 46 (2016) 1651–1662.

[24] K.W. Miller, N.V. Reo, A.J. Schoot Uiterkamp, D.P. Stengle, T.R. Stengle, K.L. Williamson, Xenon NMR: chemical shifts of a general anesthetic in common solvents, proteins, and membranes, Proc. Natl. Acad. Sci. USA 78 (1981) 4946–4949.

[25] E.J. van Beek, J.M. Wild, H.U. Kauczor, W. Schreiber, J.P. Mugler 3rd, E.E. de Lange, Functional MRI of the lung using hyperpolarized 3-helium gas, J. Magn. Reson. Imaging 20 (2004) 540–554.

[26] S. Fain, M.L. Schiebler, D.G. McCormack, G. Parraga, Imaging of lung function using hyperpolarized helium-3 magnetic resonance imaging: review of current and emerging translational methods and applications, J. Magn. Reson. Imaging 32 (2010) 1398–1408.

[27] D.A. Shea, D. Morgan, The Helium-3 Shortage: Supply, Demand, and Options for Congress, in: Congressional Research Service, 2010.

[28] J. Bousquet, N. Khaltaev, Global Surveillance, Prevention and Control of Chronic Respiratory Diseases: A Comprehensive Approach, World Health Organization, 2007.

[29] D.J. Brenner, E.J. Hall, Computed tomography–an increasing source of radiation exposure, N. Engl. J. Med. 357 (2007) 2277–2284.

[30] M. Loeve, M.H. Lequin, M. de Bruijne, I.J. Hartmann, K. Gerbrands, M. van Straten, W.C. Hop, H.A. Tiddens, Cystic fibrosis: are volumetric ultra-low-dose expiratory CT scans sufficient for monitoring related lung disease?, Radiology 253 (2009) 223–229

[31] H. Hatabu, D.C. Alsop, J. Listerud, M. Bonnet, W.B. Gefter, T2* and proton density measurement of normal human lung parenchyma using submillisecond echo time gradient echo magnetic resonance imaging, Eur. J. Radiol. 29 (1999) 245–252.

[32] J.M. Wild, H. Marshall, M. Bock, L.R. Schad, P.M. Jakob, M. Puderbach, F. Molinari, E.J. Van Beek, J. Biederer, MRI of the lung (1/3): methods, Insights Imaging 3 (2012) 345–353.

[33] M. Puderbach, C. Hintze, S. Ley, M. Eichinger, H.U. Kauczor, J. Biederer, MR imaging of the chest: a practical approach at 1.5T, Eur. J. Radiol. 64 (2007) 345–355.

[34] K.M. Johnson, S.B. Fain, M.L. Schiebler, S. Nagle, Optimized 3D ultrashort echo time pulmonary MRI, Magn. Reson. Med. 70 (2013) 1241–1250.

[35] L. Torres, J. Kammerman, A.D. Hahn, W. Zha, S.K. Nagle, K. Johnson, N. Sandbo, K. Meyer, M. Schiebler, S.B. Fain, Structure-function imaging of lung disease using ultrashort echo time MRI, Acad. Radiol. 26 (2019) 431–441.

[36] S. Rajaram, A.J. Swift, D. Capener, A. Telfer, C. Davies, C. Hill, R. Condliffe, C. Elliot, J. Hurdman, D.G. Kiely, J.M. Wild, Lung morphology assessment with balanced steady-state free precession MR imaging compared with CT, Radiology 263 (2012) 569–577.

[37] A. Voskrebenzev, J. Vogel-Claussen, Proton MRI of the lung: how to tame scarce protons and fast signal decay, J. Magn. Reson. Imaging (2020).

[38] Y. Ohno, H. Hatabu, K. Murase, T. Higashino, H. Kawamitsu, H. Watanabe, D. Takenaka, M. Fujii, K. Sugimura, Quantitative assessment of regional pulmonary perfusion in the entire lung using three-dimensional ultrafast dynamic contrast-enhanced magnetic resonance imaging: Preliminary experience in 40 subjects, J. Magn. Reson. Imaging 20 (2004) 353–365.

[39] R.R. Edelman, H. Hatabu, E. Tadamura, W. Li, P.V. Prasad, Noninvasive assessment of regional ventilation in the human lung using oxygen-enhanced magnetic resonance imaging, Nat. Med. 2 (1996) 1236–1239.

[40] G. Bauman, M. Puderbach, M. Deimling, V. Jellus, C. Chefd'hotel, J. Dinkel, C. Hintze, H.U. Kauczor, L.R. Schad, Non-contrast-enhanced perfusion and ventilation assessment of the human lung by means of fourier decomposition in proton MRI, Magn. Reson. Med. 62 (2009) 656–664.

[41] A. Comment, S. Jannin, J.N. Hyacinthe, P. Miéville, R. Sarkar, P. Ahuja, P.R. Vasos, X. Montet, F. Lazeyras, J.P. Vallée, P. Hautle, J.A. Konter, B. van den Brandt, J.P. Ansermet, R. Gruetter, G. Bodenhausen, Hyperpolarizing gases via

dynamic nuclear polarization and sublimation, Phys. Rev. Lett. 105 (2010) 018104.

[42] I.A. Nelson, T.G. Walker, Rb-Xe spin relaxation in dilute Xe mixtures, Phys. Rev. A 65 (2002).

[43] A. Sieradzan, F.A. Franz, Quenching, depolarization, and transfer of spin polarization in Rb-N2 collisions, Phys. Rev. A 25 (1982) 2985–2995.

[44] M.V. Romalis, E. Miron, G.D. Cates, Pressure broadening of Rb D-1 and D-2 lines by He-3, He-4, N-2, and Xe: Line cores and near wings, Phys. Rev. A 56 (1997) 4569–4578.

[45] J.S. Six, T. Hughes-Riley, K.F. Stupic, G.E. Pavlovskaya, T. Meersmann, Pathway to cryogen free production of hyperpolarized Krypton-83 and Xenon-129, PLoS ONE 7 (2012).

[46] P. Nikolaou, A.M. Coffey, L.L. Walkup, B.M. Gust, N. Whiting, H. Newton, S. Barcus, I. Muradyan, M. Dabaghyan, G.D. Moroz, M.S. Rosen, S. Patz, M.J. Barlow, E.Y. Chekmenev, B.M. Goodson, Near-unity nuclear polarization with an open-source Xe-129 hyperpolarizer for NMR and MRI, Proc. Natl. Acad. Sci. USA 110 (2013) 14150–14155.

[47] P. Nikolaou, A.M. Coffey, M.J. Barlow, M.S. Rosen, B.M. Goodson, E.Y. Chekmenev, Temperature-ramped 129Xe spin-exchange optical pumping, Anal. Chem. 86 (2014) 8206–8212.

[48] B. Driehuys, G.D. Cates, E. Miron, K. Sauer, D.K. Walter, W. Happer, High-volume production of laser-polarized Xe-129, Appl. Phys. Lett. 69 (1996) 1668–1670.

[49] M.S. Rosen, T.E. Chupp, K.P. Coulter, R.C. Welsh, S.D. Swanson, Polarized Xe-129 optical pumping/spin exchange and delivery system for magnetic resonance spectroscopy and imaging studies, Rev. Sci. Instrum. 70 (1999) 1546–1552.

[50] I.C. Ruset, S. Ketel, F.W. Hersman, Optical pumping system design for large production of hyperpolarized Xe-129, Phys. Rev. Lett. 96 (2006).

[51] F.W. Hersman, I.C. Ruset, S. Ketel, I. Muradian, S.D. Covrig, J. Distelbrink, W. Porter, D. Watt, J. Ketel, J. Brackett, A. Hope, S. Patz, Large production system for hyperpolarized Xe-129 for human lung imaging studies, Acad. Radiol. 15 (2008) 683–692.

[52] H. Imai, J. Fukutomi, A. Kimura, H. Fujiwara, Effect of reduced pressure on the polarization of 129Xe in the production of hyperpolarized 129Xe gas: development of a simple continuous flow mode hyperpolarizing system working at pressures as low as 0.15 atm, Concepts Magnet. Reson. Part B: Magnet. Reson. Eng. 33B (2008) 192–200.

[53] G. Norquay, S.R. Parnell, X. Xu, J. Parra-Robles, J.M. Wild, Optimized production of hyperpolarized 129Xe at 2 bars for in vivo lung magnetic resonance imaging, J. Appl. Phys. 113 (2013) 044908.

[54] M.S. Freeman, K. Emami, B. Driehuys, Characterizing and modeling the efficiency limits in large-scale production of hyperpolarized $^{129}\mathrm{Xe}$, Phys. Rev. A 90 (2014) 023406.

[55] J.R. Birchall, P. Nickolaou, A.M. Coffey, B.E. Kidd, M. Murphy, M. Molway, L.B. Bales, B.M. Goodson, R.K. Irwin, M.J. Barlow, E.Y. Chekmenev, Batch-mode clinical-scale optical hyperpolarization of xenon-129 using an aluminium jacket with rapid temperature ramping, Anal. Chem. 92 (2020) 4309–4316.

[56] J.R. Birchall, P. Nickolaou, R.K. Irwin, M.J. Barlow, K. Ranta, A.M. Coffey, B.M. Goodson, E.V. Pokochueva, K.V. Kovtunov, I.V. Koptyug, E.Y. Chekmenev, Helium-rich mixtures for improved batch-mode clinical-scale spin-exchange optical pumping of Xenon-129, J. Magn. Reson. 315 (2020) 106739.

[57] M. He, S.H. Robertson, S.S. Kaushik, M.S. Freeman, R.S. Virgincar, J. Davies, J. Stiles, W.M. Foster, H.P. McAdams, B. Driehuys, Dose and pulse sequence considerations for hyperpolarized 129Xe ventilation MRI, Magn. Reson. Imaging 33 (2015) 877–885.

[58] G. Norquay, G.J. Collier, M. Rao, N.J. Stewart, J.M. Wild, 129Xe-Rb spin-exchange optical pumping with high photon efficiency, Phys. Rev. Lett. 121 (2018) 153201.

[59] M.R. Rao, N.J. Stewart, P.D. Griffiths, G. Norquay, J.M. Wild, Imaging human brain perfusion with inhaled hyperpolarized 129Xe MR imaging, Radiology 286 (2018) 659–665.

[60] M. Rao, G. Norquay, N.J. Stewart, N. Hoggard, P.D. Griffiths, J.M. Wild, Assessment of cerebral infarction due to intracranial arterial stenosis in the human brain using hyperpolarized xenon-129 MRI, Proc. Intl. Soc. Mag. Reson. Med. 26 (2018) P 3163.

[61] W. Kilian, F. Seifert, H. Rinneberg, Dynamic NMR spectroscopy of hyperpolarized (129)Xe in human brain analyzed by an uptake model, Magn. Reson. Med. 51 (2004) 843–847.

[62] J. Chacon-Caldera, A. Maunder, M. Rao, G. Norquay, O.I. Rodgers, M. Clemence, C. Puddu, L.R. Schad, J.M. Wild, Dissolved hyperpolarized xenon-129 MRI in human kidneys, Magn. Reson. Med. 83 (2020) 262–270.

[63] L. Zhao, R. Mulkern, C.H. Tseng, D. Williamson, S. Patz, R. Kraft, R.L. Walsworth, F.A. Jolesz, M.S. Albert, Gradient-echo imaging considerations for hyperpolarized 129Xe MR, J. Magn. Reson., Ser B 113 (1996) 179–183.

[64] B. Chann, I.A. Nelson, L.W. Anderson, B. Driehuys, T.G. Walker, Xe-129-Xe molecular spin relaxation, Phys. Rev. Lett. 88 (2002).

[65] J.P. Mugler 3rd, T.A. Altes, Hyperpolarized 129Xe MRI of the human lung, J. Magn. Reson. Imaging 37 (2013) 313–331.

[66] C. Jameson, A. Jameson, Nuclear spin relaxation by intermolecular magnetic dipole coupling in the gas phase. 129Xe in oxygen, J. Chem. Phys. 89 (1988) 4074–4081.

[67] X. Xu, G. Norquay, S.R. Parnell, M.H. Deppe, S. Ajraoui, R. Hashoian, H. Marshall, P.D. Griffiths, J. Parra-Robles, J.M. Wild, Hyperpolarized 129Xe gas lung MRI-SNR and T2* comparisons at 1.5 T and 3 T, Magn. Reson. Med. 68 (2012) 1900–1904.

[69] J.M. Wild, M.N. Paley, M. Viallon, W.G. Schreiber, E.J. van Beek, P.D. Griffiths, k-space filtering in 2D gradient-echo breath-hold hyperpolarized 3He MRI: spatial resolution and signal-to-noise ratio considerations, Magn. Reson. Med. 47 (2002) 687–695.

[70] K. Nagashima, Optimum pulse flip angles for multi-scan acquisition of hyperpolarized NMR and MRI, J. Magn. Reson. 190 (2008) 183–188.

[71] H. Deng, J. Zhong, W. Ruan, X. Chen, X. Sun, C. Ye, M. Liu, X. Zhou, Constant-variable flip angles for hyperpolarized media MRI, J. Magn. Reson. 263 (2016) 92–100.

[72] M.H. Deppe, K. Teh, J. Parra-Robles, K.J. Lee, J.M. Wild, Slice profile effects in 2D slice-selective MRI of hyperpolarized nuclei, J. Magn. Reson. 202 (2010) 180–189.

[73] M. Salerno, T.A. Altes, J.R. Brookeman, E.E. de Lange, J.P. Mugler 3rd, Rapid hyperpolarized 3He diffusion MRI of healthy and emphysematous human lungs using an optimized interleaved-spiral pulse sequence, J. Magn. Reson. Imaging 17 (2003) 581–588.

[74] H. Marshall, S. Ajraoui, M.H. Deppe, J. Parra-Robles, J.M. Wild, K-space filter deconvolution and flip angle self-calibration in 2D radial hyperpolarised 3He lung MRI, NMR Biomed. 25 (2012) 389–399.

[75] J.M. Wild, S. Fichele, N. Woodhouse, M.N. Paley, L. Kasuboski, E.J. van Beek, 3D volume-localized pO2 measurement in the human lung with 3He MRI, Magn. Reson. Med. 53 (2005) 1055–1064.

[76] H. Marshall, J. Parra-Robles, M.H. Deppe, D.A. Lipson, R. Lawson, J.M. Wild, (3) He pO2 mapping is limited by delayed-ventilation and diffusion in chronic obstructive pulmonary disease, Magn. Reson. Med. 71 (2014) 1172–1178.

[77] J.M. Wild, K. Teh, N. Woodhouse, M.N. Paley, S. Fichele, N. de Zanche, L. Kasuboski, Steady-state free precession with hyperpolarized 3He: experiments and theory, J. Magn. Reson. 183 (2006) 13–24.

[78] N.J. Stewart, G. Norquay, P.D. Griffiths, J.M. Wild, Feasibility of human lung ventilation imaging using highly polarized naturally abundant xenon and optimized three-dimensional steady-state free precession, Magn. Reson. Med. 74 (2015) 346–352.

[79] J.M. Wild, N. Woodhouse, M.N. Paley, S. Fichele, Z. Said, L. Kasuboski, E.J. van Beek, Comparison between 2D and 3D gradient-echo sequences for MRI of human lung ventilation with hyperpolarized 3He, Magn. Reson. Med. 52 (2004) 673–678.

[80] J.M. Wild, M.N. Paley, L. Kasuboski, A. Swift, S. Fichele, N. Woodhouse, P.D. Griffiths, E.J. van Beek, Dynamic radial projection MRI of inhaled hyperpolarized 3He gas, Magn. Reson. Med. 49 (2003) 991–997.

[81] M. Salerno, T.A. Altes, J.R. Brookeman, E.E. de Lange, J.P. Mugler 3rd, Dynamic spiral MRI of pulmonary gas flow using hyperpolarized (3)He: preliminary studies in healthy and diseased lungs, Magn. Reson. Med. 46 (2001) 667–677.

[82] O. Doganay, T.N. Matin, A. McIntyre, B. Burns, R.F. Schulte, F.V. Gleeson, D. Bulte, Fast dynamic ventilation MRI of hyperpolarized (129) Xe using spiral imaging, Magn. Reson. Med. 79 (2018) 2597–2606.

[83] P.J. Niedbalski, M.M. Willmering, S.H. Robertson, M.S. Freeman, W. Loew, R.O. Giaquinto, C. Ireland, R.G. Pratt, C.L. Dumoulin, J.C. Woods, Z.I. Cleveland, Mapping and correcting hyperpolarized magnetization decay with radial keyhole imaging, Magn. Reson. Med. 82 (2019) 367–376.

[84] M.M. Willmering, P.J. Niedbalski, H. Wang, L.L. Walkup, R.K. Robison, J.G. Pipe, Z.I. Cleveland, J.C. Woods, Improved pulmonary (129) Xe ventilation imaging via 3D-spiral UTE MRI, Magn. Reson. Med. 84 (2020) 312–320.

[85] D.K. Sodickson, W.J. Manning, Simultaneous acquisition of spatial harmonics (SMASH): fast imaging with radiofrequency coil arrays, Magn. Reson. Med. 38 (1997) 591–603.

[86] K.P. Pruessmann, M. Weiger, M.B. Scheidegger, P. Boesiger, SENSE: sensitivity encoding for fast MRI, Magn. Reson. Med. 42 (1999) 952–962.

[87] M. Lustig, D. Donoho, J.M. Pauly, Sparse MRI: the application of compressed sensing for rapid MR imaging, Magn. Reson. Med. 58 (2007) 1182–1195.

[88] J.P. Mugler III, J.R. Brookeman, Signal-to-noise considerations for parallel imaging with hyperpolarized gases, in: International Society for Magnetic Resonance in Medicine, Miami, 2005, pp. 108.

[89] K. Teh, K.J. Lee, M.N. Paley, J.M. Wild, Parallel imaging of hyperpolarized helium-3 with simultaneous slice excitation, Magn. Reson. Med. 55 (2006) 258–262.

[90] R.F. Lee, G. Johnson, R.I. Grossman, B. Stoeckel, R. Trampel, G. McGuinness, Advantages of parallel imaging in conjunction with hyperpolarized helium–a new approach to MRI of the lung, Magn. Reson. Med. 55 (2006) 1132–1141.

[91] F.M. Meise, J. Rivoire, M. Terekhov, G.C. Wiggins, B. Keil, S. Karpuk, Z. Salhi, L. L. Wald, L.M. Schreiber, Design and evaluation of a 32-channel phased-array coil for lung imaging with hyperpolarized 3-helium, Magn. Reson. Med. 63 (2010) 456–464.

[92] M.H. Deppe, J. Parra-Robles, H. Marshall, T. Lanz, J.M. Wild, A flexible 32-channel receive array combined with a homogeneous transmit coil for human lung imaging with hyperpolarized 3He at 1.5 T, Magn. Reson. Med. 66 (2011) 1788–1797.

[93] I. Dregely, I.C. Ruset, G. Wiggins, A. Mareyam, J.P. Mugler, T.A. Altes, C. Meyer, K. Ruppert, L.L. Wald, F.W. Hersman, 32-channel phased-array receive with asymmetric birdcage transmit coil for hyperpolarized xenon-129 lung imaging, Magn. Reson. Med. (2012).

[94] G.J. Collier, P.J.C. Hughes, F.C. Horn, H.F. Chan, B. Tahir, G. Norquay, N.J. Stewart, J.M. Wild, Single breath-held acquisition of coregistered 3D (129) Xe lung ventilation and anatomical proton images of the human lung with compressed sensing, Magn. Reson. Med. 82 (2019) 342–347.

[95] H.F. Chan, N.J. Stewart, G. Norquay, G.J. Collier, J.M. Wild, 3D diffusion-weighted (129) Xe MRI for whole lung morphometry, Magn. Reson. Med. 79 (2018) 2986–2995.

[96] H. Zhang, J. Xie, S. Xiao, X. Zhao, M. Zhang, L. Shi, K. Wang, G. Wu, X. Sun, C. Ye, X. Zhou, Lung morphometry using hyperpolarized 129Xe multi-b diffusion MRI with compressed sensing in healthy subjects and patients with COPD, Med. Phys. 45 (2018) 3097–3108.

[97] S. Xiao, H. Deng, C. Duan, J. Xie, H. Zhang, X. Sun, C. Ye, X. Zhou, Considering low-rank, sparse and gas-inflow effects constraints for accelerated pulmonary dynamic hyperpolarized (129)Xe MRI, J. Magn. Reson. 290 (2018) 29–37.

[98] J. Xie, H. Li, H. Zhang, X. Zhao, L. Shi, M. Zhang, S. Xiao, H. Deng, K. Wang, H. Yang, X. Sun, G. Wu, C. Ye, X. Zhou, Single breath-hold measurement of pulmonary gas exchange and diffusion in humans with hyperpolarized (129) Xe MR, NMR Biomed. 32 (2019) e4068.

[99] S. Ajraoui, J. Parra-Robles, J.M. Wild, Incorporation of prior knowledge in compressed sensing for faster acquisition of hyperpolarized gas images, Magn. Reson. Med. 69 (2013) 360–369.

[100] G.J. Collier, J.M. Wild, In vivo measurement of gas flow in human airways with hyperpolarized gas MRI and compressed sensing, Magn. Reson. Med. 73 (2015) 2255–2261.

[101] H.F. Chan, N.J. Stewart, J. Parra-Robles, G.J. Collier, J.M. Wild, Whole lung morphometry with 3D multiple b-value hyperpolarized gas MRI and compressed sensing, Magn. Reson. Med. 77 (2017) 1916–1925.

[102] R.Y. Chen, F.C. Fan, S. Kim, K.M. Jan, S. Usami, S. Chien, Tissue-blood partition coefficient for xenon: temperature and hematocrit dependence, J. Appl. Physiol.: Resp., Environ. Exercise Physiol. 49 (1980) 178–183.

[103] X. Xu, G. Leung, G. Norquay, H. Marshall, J. Parra-Robles, J.M. Wild, T2* measurements of dissolved-phase 129Xe in the human lungs at 1.5 T and 3 T, Proc. Intl. Soc. Mag. Reson. Med. 21 (2013) 4119.

[104] K. Qing, K. Ruppert, Y. Jiang, J.F. Mata, G.W. Miller, Y.M. Shim, C. Wang, I.C. Ruset, F.W. Hersman, T.A. Altes, J.P. Mugler, Regional mapping of gas uptake by blood and tissue in the human lung using hyperpolarized xenon-129 MRI, J. Magn. Reson. Imaging 39 (2014) 346–359.

[105] Z. Wang, M. He, E. Bier, L. Rankine, G. Schrank, S. Rajagopal, Y.C. Huang, C. Kelsey, S. Womack, J. Mammarappallil, B. Driehuys, Hyperpolarized (129) Xe gas transfer MRI: the transition from 1.5T to 3T, Magn. Reson. Med. 80 (2018) 2374–2383.

[106] N.J. Stewart, G. Leung, G. Norquay, H. Marshall, J. Parra-Robles, P.S. Murphy, R. F. Schulte, C. Elliot, R. Condliffe, P.D. Griffiths, D.G. Kiely, M.K. Whyte, J. Wolber, J.M. Wild, Experimental validation of the hyperpolarized 129Xe chemical shift saturation recovery technique in healthy volunteers and subjects with interstitial lung disease, Magn. Reson. Med. 74 (2015) 196–207.

[107] Y.V. Chang, J.D. Quirk, I.C. Ruset, J.J. Atkinson, F.W. Hersman, J.C. Woods, Quantification of human lung structure and physiology using hyperpolarized 129Xe, Magn. Reson. Med. 71 (2014) 339–344.

[108] A. Bifone, Y.Q. Song, R. Seydoux, R.E. Taylor, B.M. Goodson, T. Pietrass, T.F. Budinger, G. Navon, A. Pines, NMR of laser-polarized xenon in human blood, Proc. Natl. Acad. Sci. USA 93 (1996) 12932–12936.

[109] J.P. Mugler, T.A. Altes, I.C. Ruset, I.M. Dregely, J.F. Mata, G.W. Miller, S. Ketel, J. Ketel, F.W. Hersman, K. Ruppert, Simultaneous magnetic resonance imaging of ventilation distribution and gas uptake in the human lung using hyperpolarized xenon-129, Proc. Natl. Acad. Sci. USA 107 (2010) 21707–21712.

[110] G. Leung, G. Norquay, R.F. Schulte, J.M. Wild, Radiofrequency pulse design for the selective excitation of dissolved 129Xe, Magn. Reson. Med. 73 (2015) 21–30.

[111] M.S. Albert, D. Balamore, D.F. Kacher, A.K. Venkatesh, F.A. Jolesz, Hyperpolarized 129Xe T1 in oxygenated and deoxygenated blood, NMR Biomed. 13 (2000) 407–414.

[112] J. Wolber, A. Cherubini, M.O. Leach, A. Bifone, On the oxygenation-dependent (129)Xe T (1) in blood, NMR Biomed. 13 (2000) 234–237.

[113] G. Norquay, G. Leung, N.J. Stewart, G.M. Tozer, J. Wolber, J.M. Wild, Relaxation and exchange dynamics of hyperpolarized 129Xe in human blood, Magn. Reson. Med. 74 (2015) 303–311.

[114] M. Rao, N.J. Stewart, G. Norquay, P.D. Griffiths, J.M. Wild, High resolution spectroscopy and chemical shift imaging of hyperpolarized 129 Xe dissolved in the human brain in vivo at 1.5 tesla, Magn. Reson. Med. 75 (2016) 2227–2234.

[115] F.T. Hane, H. Imai, A. Kimura, H. Fujiwara, M. Rao, J.M. Wild, M.S. Albert, Chapter 16 - Brain Imaging Using Hyperpolarized Xenon MRI, in: Hyperpolarized and Inert Gas MRI, Academic Press, Boston, 2017, pp. 251–262.

[116] W.M. Haynes, CRC Handbook of Chemistry and Physics, 96th ed., CRC Press, 2015.

[117] D.I. Hoult, P.C. Lauterbur, The sensitivity of the zeugmatographic experiment involving human samples, J. Magn. Reson. (1969) 34 (1979) 425–433.

[118] D.G. Gadian, F.N.H. Robinson, Radiofrequency losses in NMR experiments on electrically conducting samples, J. Magn. Reson. (1969) 34 (1979) 449–455.

[119] T.W. Redpath, J.M.S. Hutchison, Estimating patient dielectric losses in NMR imagers, Magn. Reson. Imaging 2 (1984) 295–300.

[120] K.M. Gilbert, T.J. Scholl, B.A. Chronik, RF coil loading measurements between 1 and 50 MHz to guide field-cycled MRI system design, Concepts Magnet. Reson. Part B: Magnet. Reson. Eng. 33B (2008) 177–191.

[121] J.W. Carlson, Radiofrequency field propagation in conductive NMR samples, J. Magn. Reson. (1969) 78 (1988) 563–573.

[122] D.I. Hoult, Sensitivity and power deposition in a high-field imaging experiment, J. Magn. Reson. Imaging 12 (2000) 46–67.

[123] C.E. Hayes, W.A. Edelstein, J.F. Schenck, O.M. Mueller, M. Eash, An efficient, highly homogeneous radiofrequency coil for whole-body NMR imaging at 1.5 T, J. Magn. Reson. (1969) 63 (1985) 622–628.

[124] F.D. Doty, G. Entzminger Jr, C.D. Hauck, J.P. Staab, Practical aspects of birdcage coils, J. Magn. Reson. (1969) 138 (1999) 144–154.

[125] W.A. Edelstein, P.A. Bottomley, H.R. Hart, L.S. Smith, Signal, noise, and contrast in nuclear magnetic resonance (NMR) imaging, J. Comput. Assist. Tomogr. 7 (1983) 391–401.

[126] W.A. Edelstein, P.A. Bottomley, L.M. Pfeifer, A signal-to-noise calibration procedure for NMR imaging systems, Med. Phys. 11 (1984) 180–185.

[127] O. Ocali, E. Atalar, Ultimate intrinsic signal-to-noise ratio in MRI, Magn. Reson. Med. 39 (1998) 462–473.

[128] B. Roemer, W.A. Edelstein, Nuclear magnetic resonance (NMR) imaging with multiple surface coils, US patent: US4825162A, 1989.

[129] R.F. Lee, G. Johnson, B. Stoeckel, C. Stefanescu, R. Trampel, G. McGuinness, A 24-ch phased-array system for hyperpolarized helium gas parallel MRI to evaluate lung functions, 2005, pp. 4278–4281.

[130] N. De Zanche, N. Chhina, K. Teh, C. Randell, K.P. Pruessmann, J.M. Wild, Asymmetric quadrature split birdcage coil for hyperpolarized 3He lung MRI at 1.5T, Magn. Reson. Med. 60 (2008) 431–438.

[131] N. De Zanche, A. Yahya, F.E. Vermeulen, P.S. Allen, Analytical approach to noncircular section birdcage coil design: verification with a cassinian oval coil, Magn. Reson. Med. 53 (2005) 201–211.

[132] L.F. Donnelly, J.R. MacFall, H.P. McAdams, J.M. Majure, J. Smith, D.P. Frush, P. Bogonad, H.C. Charles, C.E. Ravin, Cystic fibrosis: Combined hyperpolarized 3He-enhanced and conventional proton MR imaging in the lung – preliminary observations, Radiology 212 (1999) 885–889.

[133] N. Woodhouse, J.M. Wild, M.N. Paley, S. Fichele, Z. Said, A.J. Swift, E.J. van Beek, Combined helium-3/proton magnetic resonance imaging measurement of ventilated lung volumes in smokers compared to never-smokers, J. Magn. Reson. Imaging 21 (2005) 365–369.

[134] J. Zheng, J.C. Leawoods, M. Nolte, D.A. Yablonskiy, P.K. Woodard, G. Laub, R.J. Gropler, M.S. Conradi, Combined MR proton lung perfusion/angiography and helium ventilation: potential for detecting pulmonary emboli and ventilation defects, Magn. Reson. Med. 47 (2002) 433–438.

[135] J.M. Wild, S. Ajraoui, M.H. Deppe, S.R. Parnell, H. Marshall, J. Parra-Robles, R. H. Ireland, Synchronous acquisition of hyperpolarised 3He and 1H MR images of the lungs – maximising mutual anatomical and functional information, NMR Biomed. 24 (2011) 130–134.

[136] J.M. Wild, H. Marshall, X. Xu, G. Norquay, S.R. Parnell, M. Clemence, P.D. Griffiths, J. Parra-Robles, Simultaneous imaging of lung structure and function with triple-nuclear hybrid MR imaging, Radiology 267 (2013) 251–255.

[137] F.C. Horn, B.A. Tahir, N.J. Stewart, G.J. Collier, G. Norquay, G. Leung, R.H. Ireland, J. Parra-Robles, H. Marshall, J.M. Wild, Lung ventilation volumetry with same-breath acquisition of hyperpolarized gas and proton MRI, NMR Biomed. 27 (2014) 1461–1467.

[138] N.J. Tustison, B.B. Avants, Z. Lin, X. Feng, N. Cullen, J.F. Mata, L. Flors, J.C. Gee, T.A. Altes, J.P. Mugler Iii, K. Qing, Convolutional neural networks with template-based data augmentation for functional lung image quantification, Acad. Radiol. 26 (2019) 412–423.

[139] A.W. Magill, R. Gruetter, Nested Surface Coils for Multinuclear NMR, in: eMagRes, John Wiley & Sons, Ltd, 2007.

[140] G.X. Shen, F.E. Boada, K.R. Thulborn, Dual-frequency, dual-quadrature, birdcage RF coil design with identical B1 pattern for sodium and proton imaging of the human brain at 1.5 T, Magn. Reson. Med. 38 (1997) 717–725.

[141] G.B. Matson, P. Vermathen, T.C. Hill, A practical double-tuned 1H/31P quadrature birdcage headcoil optimized for 31P operation, Magn. Reson. Med. 42 (1999) 173–182.

[142] A.R. Rath, Design and performance of a double-tuned bird-cage coil, J. Magn. Reson. (1969) 86 (1990) 488–495.

[143] G. Isaac, M.D. Schnall, R.E. Lenkinski, K. Vogele, A design for a double-tuned birdcage coil for use in an integrated MRI/MRS examination, J. Magn. Reson. (1969) 89 (1990) 41–50.

[144] M. Rao, F. Robb, J.M. Wild, Dedicated receiver array coil for 1H lung imaging with same-breath acquisition of hyperpolarized 3He and 129Xe gas, Magn. Reson. Med. 74 (2015) 291–299.

[145] M. Rao, J.M. Wild, RF instrumentation for same-breath triple nuclear lung MR imaging of (1)H and hyperpolarized (3)He and (129)Xe at 1.5T, Magn. Reson. Med. 75 (2016) 1841–1848.

[146] S. Ha, M.J. Hamamura, O. Nalcioglu, L.T. Muftuler, A PIN diode controlled dual-tuned MRI RF coil and phased array for multi nuclear imaging, Phys. Med. Biol. 55 (2010) 2589–2600.

[147] A. Maunder, M. Rao, F. Robb, J.M. Wild, Comparison of MEMS switches and PIN diodes for switched dual tuned RF coils, Magn. Reson. Med. 80 (2018) 1746–1753.

[148] M. Kirby, M. Heydarian, S. Svenningsen, A. Wheatley, D.G. McCormack, R. Etemad-Rezai, G. Parraga, Hyperpolarized 3He magnetic resonance functional imaging semiautomated segmentation, Acad. Radiol. 19 (2012) 141–152.

[149] R.S. Virgincar, Z.I. Cleveland, S.S. Kaushik, M.S. Freeman, J. Nouls, G.P. Cofer, S. Martinez-Jimenez, M. He, M. Kraft, J. Wolber, H.P. McAdams, B. Driehuys, Quantitative analysis of hyperpolarized 129Xe ventilation imaging in healthy

volunteers and subjects with chronic obstructive pulmonary disease, NMR Biomed. 26 (2013) 424–435.

[150] M. He, S.S. Kaushik, S.H. Robertson, M.S. Freeman, R.S. Virgincar, H.P. McAdams, B. Driehuys, Extending semiautomatic ventilation defect analysis for hyperpolarized (129)Xe ventilation MRI, Acad. Radiol. 21 (2014) 1530–1541.

[151] M. He, B. Driehuys, L.G. Que, Y.T. Huang, Using Hyperpolarized (129)Xe MRI to quantify the pulmonary ventilation distribution, Acad. Radiol. 23 (2016) 1521–1531.

[152] P.J.C. Hughes, F.C. Horn, G.J. Collier, A. Biancardi, H. Marshall, J.M. Wild, Spatial fuzzy c-means thresholding for semiautomated calculation of percentage lung ventilated volume from hyperpolarized gas and (1) H MRI, J. Magn. Reson. Imaging 47 (2018) 640–646.

[153] T.N. Matin, N. Rahman, A.H. Nickol, M. Chen, X. Xu, N.J. Stewart, T. Doel, V. Grau, J.M. Wild, F.V. Gleeson, Chronic obstructive pulmonary disease: lobar analysis with hyperpolarized (129)Xe MR imaging, Radiology 282 (2017) 857–868.

[154] M. He, W. Zha, F. Tan, L. Rankine, S. Fain, B. Driehuys, A comparison of two hyperpolarized (129)Xe MRI ventilation quantification pipelines: the effect of signal to noise ratio, Acad. Radiol. (2018).

[155] L. Ebner, M. He, R.S. Virgincar, T. Heacock, S.S. Kaushik, M.S. Freemann, H.P. McAdams, M. Kraft, B. Driehuys, Hyperpolarized 129Xenon magnetic resonance imaging to quantify regional ventilation differences in mild to moderate asthma: a prospective comparison between semiautomated ventilation defect percentage calculation and pulmonary function tests, Invest. Radiol. 52 (2017) 120–127.

[156] N. Kanhere, M.J. Couch, K. Kowalik, B. Zanette, J.H. Rayment, D. Manson, P. Subbarao, F. Ratjen, G. Santyr, Correlation of lung clearance index with hyperpolarized (129)Xe magnetic resonance imaging in pediatric subjects with cystic fibrosis, Am. J. Respir. Crit. Care Med. 196 (2017) 1073–1075.

[157] N.J. Stewart, H.F. Chan, P.J.C. Hughes, F.C. Horn, G. Norquay, M. Rao, D.P. Yates, R.H. Ireland, M.Q. Hatton, B.A. Tahir, P. Ford, A.J. Swift, R. Lawson, H. Marshall, G.J. Collier, J.M. Wild, Comparison of (3) He and (129) Xe MRI for evaluation of lung microstructure and ventilation at 1.5T, J. Magn. Reson. Imaging (2018).

[158] G. Santyr, N. Kanhere, F. Morgado, J.H. Rayment, F. Ratjen, M.J. Couch, Hyperpolarized gas magnetic resonance imaging of pediatric cystic fibrosis lung disease, Acad. Radiol. (2018).

[159] M. Kirby, S. Svenningsen, A. Owrangi, A. Wheatley, A. Farag, A. Ouriadov, G.E. Santyr, R. Etemad-Rezai, H.O. Coxson, D.G. McCormack, G. Parraga, Hyperpolarized 3He and 129Xe MR imaging in healthy volunteers and patients with chronic obstructive pulmonary disease, Radiology 265 (2012) 600–610.

[160] O. Doganay, T. Matin, M. Chen, M. Kim, A. McIntyre, D.R. McGowan, K.M. Bradley, T. Povey, F.V. Gleeson, Time-series hyperpolarized xenon-129 MRI of lobar lung ventilation of COPD in comparison to V/Q-SPECT/CT and CT, Eur. Radiol. 29 (2019) 4058–4067.

[161] B.A. Tahir, P.J.C. Hughes, S.D. Robinson, H. Marshall, N.J. Stewart, G. Norquay, A. Biancardi, H.F. Chan, G.J. Collier, K.A. Hart, J.A. Swinscoe, M.Q. Hatton, J.M. Wild, R.H. Ireland, Spatial comparison of CT-based surrogates of lung ventilation with hyperpolarized helium-3 and Xenon-129 gas MRI in patients undergoing radiation therapy, Int. J. Radiat. Oncol. Biol. Phys. 102 (2018) 1276–1286.

[162] Y.S. Tzeng, K. Lutchen, M. Albert, The difference in ventilation heterogeneity between asthmatic and healthy subjects quantified using hyperpolarized 3He MRI, J. Appl. Physiol. (1985) 106 (2009) 813–822.

[163] S. Svenningsen, M. Kirby, D. Starr, D. Leary, A. Wheatley, G.N. Maksym, D.G. McCormack, G. Parraga, Hyperpolarized (3) He and (129) Xe MRI: differences in asthma before bronchodilation, J. Magn. Reson. Imaging 38 (2013) 1521–1530.

[164] L. Ebner, R.S. Virgincar, M. He, K.R. Choudhury, S.H. Robertson, A. Christe, A. Mileto, J.G. Mammarapallil, H.P. McAdams, B. Driehuys, J.E. Roos, Multireader determination of clinically significant obstruction using hyperpolarized (129) Xe-ventilation MRI, AJR Am. J. Roentgenol. 212 (2019) 758–765.

[165] R.P. Thomen, L.L. Walkup, D.J. Roach, Z.I. Cleveland, J.P. Clancy, J.C. Woods, Hyperpolarized (129)Xe for investigation of mild cystic fibrosis lung disease in pediatric patients, J. Cyst. Fibros. 16 (2017) 275–282.

[166] M.J. Couch, R. Thomen, N. Kanhere, R. Hu, F. Ratjen, J. Woods, G. Santyr, A two-center analysis of hyperpolarized (129)Xe lung MRI in stable pediatric cystic fibrosis: potential as a biomarker for multi-site trials, J. Cyst. Fibros. 18 (2019) 728–733.

[167] R.P. Thomen, L.L. Walkup, D.J. Roach, N. Higano, A. Schapiro, A. Brody, J.P. Clancy, Z.I. Cleveland, J.C. Woods, Regional structure-function in cystic fibrosis lung disease using hyperpolarized (129)Xe and ultrashort echo magnetic resonance imaging, Am. J. Respir. Crit. Care Med. (2020).

[168] L.L. Walkup, D.J. Roach, C.S. Hall, N. Gupta, R.P. Thomen, Z.I. Cleveland, F.X. McCormack, J.C. Woods, Cyst ventilation heterogeneity and alveolar airspace dilation as early disease markers in lymphangioleiomyomatosis, Ann. Am. Thorac. Soc. 16 (2019) 1008–1016.

[169] L.L. Walkup, K. Myers, J. El-Bietar, A. Nelson, M.M. Willmering, M. Grimley, S. M. Davies, C. Towe, J.C. Woods, Xenon-129 MRI detects ventilation deficits in paediatric stem cell transplant patients unable to perform spirometry, Eur. Respir. J. 53 (2019).

[170] J.H. Rayment, M.J. Couch, N. McDonald, N. Kanhere, D. Manson, G. Santyr, F. Ratjen, Hyperpolarised (129)Xe magnetic resonance imaging to monitor treatment response in children with cystic fibrosis, Eur. Respir. J. 53 (2019).

[171] K. Mahmood, L. Ebner, M. He, S.H. Robertson, Z. Wang, H.P. McAdams, M.M. Wahidi, S.L. Shofer, Y.T. Huang, B. Driehuys, Novel magnetic resonance imaging for assessment of bronchial stenosis in lung transplant recipients, Am. J. Transplant. 17 (2017) 1895–1904.

[172] E.J. Song, C.R. Kelsey, B. Driehuys, L. Rankine, Functional airway obstruction observed with hyperpolarized (129) Xenon-MRI, J. Med. Imaging Radiat. Oncol. 62 (2018) 91–93.

[173] I. Muradyan, S.H. Loring, M. Ferrigno, P. Lindholm, G.P. Topulos, S. Patz, J.P. Butler, Inhalation heterogeneity from subresidual volumes in elite divers, J. Appl. Physiol. (1985) 109 (2010) 1969–1973.

[174] P.J.C. Hughes, L. Smith, H.F. Chan, B.A. Tahir, G. Norquay, G.J. Collier, A. Biancardi, H. Marshall, J.M. Wild, Assessment of the influence of lung inflation state on the quantitative parameters derived from hyperpolarized gas lung ventilation MRI in healthy volunteers, J. Appl. Physiol. (1985) 126 (2019) 183–192.

[175] M. Kirby, S. Svenningsen, N. Kanhere, A. Owrangi, A. Wheatley, H.O. Coxson, G.E. Santyr, N.A. Paterson, D.G. McCormack, G. Parraga, Pulmonary ventilation visualized using hyperpolarized helium-3 and xenon-129 magnetic resonance imaging: differences in COPD and relationship to emphysema, J. Appl. Physiol. (1985) 114 (2013) 707–715.

[176] X.J. Chen, H.E. Moller, M.S. Chawla, G.P. Cofer, B. Driehuys, L.W. Hedlund, G.A. Johnson, Spatially resolved measurements of hyperpolarized gas properties in the lung in vivo. Part I: diffusion coefficient, Magn. Reson. Med. 42 (1999) 721–728.

[177] H. Marshall, G.J. Collier, C.S. Johns, H.F. Chan, G. Norquay, R.A. Lawson, J.M. Wild, Imaging collateral ventilation in patients with advanced chronic obstructive pulmonary disease: relative sensitivity of (3) He and (129) Xe MRI, J. Magn. Reson. Imaging (2018).

[178] M. Chen, O. Doganay, T. Matin, A. McIntyre, N. Rahman, D. Bulte, F. Gleeson, Delayed ventilation assessment using fast dynamic hyperpolarised Xenon-129 magnetic resonance imaging, Eur. Radiol. 30 (2020) 1145–1155.

[179] F.C. Horn, M. Rao, N.J. Stewart, J.M. Wild, Multiple breath washout of hyperpolarized (129) Xe and (3) He in human lungs with three-dimensional balanced steady-state free-precession imaging, Magn. Reson. Med. 77 (2017) 2288–2295.

[180] E.R. Weibel, Morphometry of the Human Lung, Springer, 1963.

[181] E.O. Stejskal, J.E. Tanner, Spin diffusion measurements: spin echoes in the presence of a time-dependent field gradient, J. Chem. Phys. 42 (1965) 288.

[182] J.P. Mugler III, J.F. Mata, H.-T.J. Wang, W.A. Tobias, G.D. Cates, J.M. Christopher, J.L. Missel, A.G. Reish, K. Ruppert, J.R. Brookeman, K.D. Hagspiel, The apparent diffusion coefficient of Xe-129 in the lung: preliminary human results, in: Proc. Intl. Soc. Mag. Reson. Med., 2004, pp. 769.

[183] A. Sindile, I. Muradian, M. Hrovat, C. Johnson, F.W. Hersman, S. Patz, Human pulmonary diffusion weighted imaging at 0.2T with hyperpolarized 129Xe, in: Proc. Intl. Soc. Mag. Reson. Med., 2007, pp. 1290.

[184] S.S. Kaushik, Z.I. Cleveland, G.P. Cofer, G. Metz, D. Beaver, J. Nouls, M. Kraft, W. Auffermann, J. Wolber, H.P. McAdams, B. Driehuys, Diffusion-weighted hyperpolarized 129Xe MRI in healthy volunteers and subjects with chronic obstructive pulmonary disease, Magn. Reson. Med. 65 (2011) 1154–1165.

[185] M. Kirby, A. Ouriadov, S. Svenningsen, A. Owrangi, A. Wheatley, R. Etemad-Rezai, G.E. Santyr, D.G. McCormack, G. Parraga, Hyperpolarized 3He and 129Xe magnetic resonance imaging apparent diffusion coefficients: physiological relevance in older never- and ex-smokers, Physiol. Rep. 2 (2014).

[186] B.T. Saam, D.A. Yablonskiy, V.D. Kodibagkar, J.C. Leawoods, D.S. Gierada, J.D. Cooper, S.S. Lefrak, M.S. Conradi, MR imaging of diffusion of 3He gas in healthy and diseased lungs, Magn. Reson. Med. 44 (2000) 174–179.

[187] M. Salerno, E.E. de Lange, T.A. Altes, J.D. Truwit, J.R. Brookeman, J.P. Mugler 3rd, Emphysema: hyperpolarized helium 3 diffusion MR imaging of the lungs compared with spirometric indexes–initial experience, Radiology 222 (2002) 252–260.

[188] K. Ruppert, K. Qing, J.T. Patrie, T.A. Altes, J.P. Mugler 3rd, Using hyperpolarized xenon-129 MRI to quantify early-stage lung disease in smokers, Acad. Radiol. 26 (2019) 355–366.

[189] H.F. Chan, G.J. Collier, N.D. Weatherley, J.M. Wild, Comparison of in vivo lung morphometry models from 3D multiple b-value (3) He and (129) Xe diffusion-weighted MRI, Magn. Reson. Med. 81 (2019) 2959–2971.

[190] R.P. Thomen, J.D. Quirk, D. Roach, T. Egan-Rojas, K. Ruppert, R.D. Yusen, T.A. Altes, D.A. Yablonskiy, J.C. Woods, Direct comparison of (129) Xe diffusion measurements with quantitative histology in human lungs, Magn. Reson. Med. 77 (2017) 265–272.

[191] J.F. Mata, T.A. Altes, J. Cai, K. Ruppert, W. Mitzner, K.D. Hagspiel, B. Patel, M. Salerno, J.R. Brookeman, E.E. de Lange, W.A. Tobias, H.T. Wang, G.D. Cates, J.P. Mugler 3rd, Evaluation of emphysema severity and progression in a rabbit model: comparison of hyperpolarized 3He and 129Xe diffusion MRI with lung morphometry, J. Appl. Physiol. (1985) 102 (2007) 1273–1280.

[192] K. Wang, T. Pan, H. Yang, W. Ruan, J. Zhong, G. Wu, X. Zhou, Assessment of pulmonary microstructural changes by hyperpolarized (129)Xe diffusion-weighted imaging in an elastase-instilled rat model of emphysema, J. Thorac. Dis. 9 (2017) 2572–2578.

[193] J. Parra-Robles, S. Ajraoui, H. Marshall, M.H. Deppe, X. Xu, J.M. Wild, The influence of field strength on the apparent diffusion coefficient of 3He gas in human lungs, Magn. Reson. Med. 67 (2012) 322–325.

[194] P. Komlosi, T.A. Altes, K. Qing, K.E. Mooney, G.W. Miller, J.F. Mata, E.E. de Lange, W.A. Tobias, G.D. Cates Jr., J.R. Brookeman, J.P. Mugler 3rd, Regional

anisotropy of airspace orientation in the lung as assessed with hyperpolarized helium-3 diffusion MRI, J. Magn. Reson. Imaging 42 (2015) 1777–1782.

[195] S. Fichele, M.N. Paley, N. Woodhouse, P.D. Griffiths, E.J. van Beek, J.M. Wild, Investigating 3He diffusion NMR in the lungs using finite difference simulations and in vivo PGSE experiments, J. Magn. Reson. 167 (2004) 1–11.

[196] D.S. Gierada, J.C. Woods, A.J. Bierhals, S.T. Bartel, J.H. Ritter, C.K. Choong, N.A. Das, C. Hong, T.K. Pilgram, Y.V. Chang, R.E. Jacob, J.C. Hogg, R.J. Battafarano, A.D. Cooper, B.F. Meyers, G.A. Patterson, D.A. Yablonskiy, M.S. Conradi, Effects of diffusion time on short-range hyperpolarized (3)He diffusivity measurements in emphysema, J. Magn. Reson. Imaging 30 (2009) 801–808.

[197] S. Ajraoui, J. Parra-Robles, M. Deppe, K. Teh, S. Parnell, J. Owers-Bradley, J. Wild, Experimental investigation of non-gaussian diffusion in hyperpolarized 3He MRI of lungs, in: Proc Int Soc Magn Reson Med, 2009, pp. 2178.

[198] D.A. Yablonskiy, A.L. Sukstanskii, J.C. Leawoods, D.S. Gierada, G.L. Bretthorst, S.S. Lefrak, J.D. Cooper, M.S. Conradi, Quantitative in vivo assessment of lung microstructure at the alveolar level with hyperpolarized 3He diffusion MRI, Proc. Natl. Acad. Sci. USA 99 (2002) 3111–3116.

[199] A.L. Sukstanskii, D.A. Yablonskiy, In vivo lung morphometry with hyperpolarized 3He diffusion MRI: theoretical background, J. Magn. Reson. 190 (2008) 200–210.

[200] D.A. Yablonskiy, A.L. Sukstanskii, J.C. Woods, D.S. Gierada, J.D. Quirk, J.C. Hogg, J.D. Cooper, M.S. Conradi, Quantification of lung microstructure with hyperpolarized 3He diffusion MRI, J. Appl. Physiol. 107 (2009) (1985) 1258–1265.

[201] A.L. Sukstanskii, D.A. Yablonskiy, Lung morphometry with hyperpolarized 129Xe: theoretical background, Magn. Reson. Med. 67 (2012) 856–866.

[202] J.M. Perez-Sanchez, I. Rodriguez, J. Ruiz-Cabello, Random walk simulation of the MRI apparent diffusion coefficient in a geometrical model of the acinar tree, Biophys. J . 97 (2009) 656–664.

[203] S. Fichele, M.N. Paley, N. Woodhouse, P.D. Griffiths, E.J. Van Beek, J.M. Wild, Finite-difference simulations of 3He diffusion in 3D alveolar ducts: comparison with the "cylinder model", Magn. Reson. Med. 52 (2004) 917–920.

[204] D.S. Grebenkov, G. Guillot, B. Sapoval, Restricted diffusion in a model acinar labyrinth by NMR: theoretical and numerical results, J. Magn. Reson. 184 (2007) 143–156.

[205] D. Habib, D. Grebenkov, G. Guillot, Gas diffusion in a pulmonary acinus model: experiments with hyperpolarized helium-3, Magn. Reson. Imaging 26 (2008) 1101–1113.

[206] R. Mair, G. Wong, D. Hoffmann, M. Hürlimann, S. Patz, L. Schwartz, R. Walsworth, Probing porous media with gas diffusion NMR, Phys. Rev. Lett. 83 (1999) 3324–3327.

[207] G.W. Miller, M. Carl, J.F. Mata, G.D. Cates Jr., J.P. Mugler 3rd, Simulations of short-time diffusivity in lung airspaces and implications for S/V measurements using hyperpolarized-gas MRI, IEEE Trans. Med. Imaging 26 (2007) 1456–1463.

[208] D.D. Shanbhag, T.A. Altes, G.W. Miller, J.F. Mata, J. Knight-Scott, q-Space analysis of lung morphometry in vivo with hyperpolarized 3He spectroscopy, J. Magn. Reson. Imaging 24 (2006) 84–94.

[209] R.L. O'Halloran, J.H. Holmes, Y.C. Wu, A. Alexander, S.B. Fain, Helium-3 MR q-space imaging with radial acquisition and iterative highly constrained back-projection, Magn. Reson. Med. 63 (2010) 41–50.

[210] R. Trampel, J.H. Jensen, R.F. Lee, I. Kamenetskiy, G. McGuinness, G. Johnson, Diffusional kurtosis imaging in the lung using hyperpolarized 3He, Magn. Reson. Med. 56 (2006) 733–737.

[211] J. Parra-Robles, H. Marshall, R. Hartley, C.E. Brightling, J. Wild, Quantification of lung microstructure in asthma using a 3He fractional diffusion approach, in: Proc. Intl. Soc. Mag. Reson. Med., 2014, pp. 3529.

[212] B. Haefeli-Bleuer, E.R. Weibel, Morphometry of the human pulmonary acinus, Anatomical Rec. 220 (1988) 401–414.

[213] M.N. Berberan-Santos, E.N. Bodunov, B. Valeur, Mathematical functions for the analysis of luminescence decays with underlying distributions 1. Kohlrausch decay function (stretched exponential), Chem. Phys. 315 (2005) 171–182.

[214] K. Ruppert, J.D. Quirk, J.P.M. III, T.A. Altes, C. Wang, G.W. Miller, I.C. Ruset, J.F. Mata, F.W. Hersman, D.A. Yablonskiy, Lung morphometry using hyperpolarized xenon-129: preliminary experience, in: Proc Intl Soc Mag Reson Med, 2012, pp. 3152.

[215] A. Ouriadov, A. Farag, M. Kirby, D.G. McCormack, G. Parraga, G.E. Santyr, Lung morphometry using hyperpolarized (129) Xe apparent diffusion coefficient anisotropy in chronic obstructive pulmonary disease, Magn. Reson. Med. 70 (2013) 1699–1706.

[216] A. Ouriadov, A. Farag, M. Kirby, D.G. McCormack, G. Parraga, G.E. Santyr, Pulmonary hyperpolarized Xe morphometry for mapping xenon gas concentrations and alveolar oxygen partial pressure: Proof-of-concept demonstration in healthy and COPD subjects, Magn. Reson. Med. 74 (2015) 1726–1732.

[217] M. Boudreau, X. Xu, G.E. Santyr, Measurement of 129Xe gas apparent diffusion coefficient anisotropy in an elastase-instilled rat model of emphysema, Magn. Reson. Med. 69 (2013) 211–220.

[218] W. Ruan, J. Zhong, K. Wang, G. Wu, Y. Han, X. Sun, C. Ye, X. Zhou, Detection of the mild emphysema by quantification of lung respiratory airways with hyperpolarized xenon diffusion MRI, J. Magn. Reson. Imaging 45 (2017) 879–888.

[219] A. Ouriadov, M. Fox, E. Hegarty, G. Parraga, E. Wong, G.E. Santyr, Early stage radiation-induced lung injury detected using hyperpolarized (129) Xe Morphometry: proof-of-concept demonstration in a rat model, Magn. Reson. Med. 75 (2016) 2421–2431.

[220] K. Sakai, A.M. Bilek, E. Oteiza, R.L. Walsworth, D. Balamore, F.A. Jolesz, M.S. Albert, Temporal dynamics of hyperpolarized129Xe resonances in living rats, J. Magnetic Reson. - Series B 111 (1996) 300–304.

[221] M.E. Wagshul, T.M. Button, H.F. Li, Z. Liang, C.S. Springer, K. Zhong, A. Wishnia, In vivo MR imaging and spectroscopy using hyperpolarized129Xe, Magn. Reson. Med. 36 (1996) 183–191.

[222] J.P. Mugler 3rd, B. Driehuys, J.R. Brookeman, G.D. Cates, S.S. Berr, R.G. Bryant, T.M. Daniel, E.E. de Lange, J.H. Downs 3rd, C.J. Erickson, W. Happer, D.P. Hinton, N.F. Kassel, T. Maier, C.D. Phillips, B.T. Saam, K.L. Sauer, M.E. Wagshul, MR imaging and spectroscopy using hyperpolarized 129Xe gas: preliminary human results, Magn. Reson. Med. 37 (1997) 809–815.

[223] J. Wolber, A. Cherubini, A.S. Dzik-Jurasz, M.O. Leach, A. Bifone, Spin-lattice relaxation of laser-polarized xenon in human blood, Proc. Natl. Acad. Sci. USA 96 (1999) 3664–3669.

[224] K. Ruppert, J.R. Brookeman, K.D. Hagspiel, B. Driehuys, J.P. Mugler, NMR of hyperpolarized 129Xe in the canine chest: spectral dynamics during a breath-hold, NMR Biomed. 13 (2000) 220–228.

[225] S. Mansson, J. Wolber, B. Driehuys, P. Wollmer, K. Golman, Characterization of diffusing capacity and perfusion of the rat lung in a lipopolysaccharide disease model using hyperpolarized 129Xe, Magn. Reson. Med. 50 (2003) 1170–1179.

[226] B. Driehuys, G.P. Cofer, J. Pollaro, J.B. Mackel, L.W. Hedlund, G.A. Johnson, Imaging alveolar-capillary gas transfer using hyperpolarized Xe-129 MRI, Proc. Natl. Acad. Sci. USA 103 (2006) 18278–18283.

[227] S. Patz, I. Muradyan, M.I. Hrovat, M. Dabaghyan, G.R. Washko, H. Hatabu, J.P. Butler, Diffusion of hyperpolarized (129)Xe in the lung: a simplified model of (129)Xe septal uptake and experimental results, New J. Phys. 13 (2011).

[228] S. Patz, I. Muradian, M.I. Hrovat, I.C. Ruset, G. Topulos, S.D. Covrig, E. Frederick, H. Hatabu, F.W. Hersman, J.P. Butler, Human pulmonary imaging and spectroscopy with hyperpolarized 129Xe at 0.2T, Acad. Radiol. 15 (2008) 713–727.

[229] Y.V. Chang, MOXE: a model of gas exchange for hyperpolarized 129Xe magnetic resonance of the lung, Magn. Reson. Med. 69 (2013) 884–890.

[230] H. Imai, A. Kimura, S. Iguchi, Y. Hori, S. Masuda, H. Fujiwara, Noninvasive detection of pulmonary tissue destruction in a mouse model of emphysema using hyperpolarized 129Xe MRS under spontaneous respiration, Magn. Reson. Med. 64 (2010) 929–938.

[231] N.J. Stewart, F.C. Horn, G. Norquay, G.J. Collier, D.P. Yates, R. Lawson, H. Marshall, J.M. Wild, Reproducibility of quantitative indices of lung function and microstructure from129Xe chemical shift saturation recovery (CSSR) MR spectroscopy, Magn. Reson. Med. 77 (2017) 2107–2113.

[232] K. Qing, J.P. Mugler, T.A. Altes, Y. Jiang, J.F. Mata, G.W. Miller, I.C. Ruset, F.W. Hersman, K. Ruppert, Assessment of lung function in asthma and COPD using hyperpolarized 129Xe chemical shift saturation recovery spectroscopy and dissolved-phase MR imaging, NMR Biomed. 27 (2014) 1490–1501.

[233] S.S. Kaushik, M.S. Freeman, S.W. Yoon, M.G. Liljeroth, J.V. Stiles, J.E. Roos, W.S. Michael Foster, C.R. Rackley, H.P. McAdams, B. Driehuys, Measuring diffusion limitation with a perfusion-limited gas—Hyperpolarized (129)Xe gas-transfer spectroscopy in patients with idiopathic pulmonary fibrosis, J. Appl. Physiol. 117 (2014) 577–585.

[234] N.D. Weatherley, N.J. Stewart, H.F. Chan, M. Austin, L.J. Smith, G. Collier, M. Rao, H. Marshall, G. Norquay, S.A. Renshaw, S.M. Bianchi, J.M. Wild, Hyperpolarised xenon magnetic resonance spectroscopy for the longitudinal assessment of changes in gas diffusion in IPF, Thorax 74 (2019) 500–502.

[235] S.H. Robertson, R.S. Virgincar, E.A. Bier, M. He, G.M. Schrank, R.M. Smigla, C. Rackley, H.P. McAdams, B. Driehuys, Uncovering a third dissolved-phase 129 Xe resonance in the human lung: Quantifying spectroscopic features in healthy subjects and patients with idiopathic pulmonary fibrosis, Magn. Reson. Med. 78 (2017) 1306–1315.

[236] R.S. Virgincar, S.H. Robertson, J. Nouls, S. Degan, G.M. Schrank, M. He, B. Driehuys, Establishing an accurate gas phase reference frequency to quantify 129Xe chemical shifts in vivo, Magn. Reson. Med. 77 (2017) 1438–1445.

[237] G. Norquay, G. Leung, N.J. Stewart, J. Wolber, J.M. Wild, 129Xe chemical shift in human blood and pulmonary blood oxygenation measurement in humans using hyperpolarized 129Xe NMR, Magn. Reson. Med. 77 (2017) 1399–1408.

[238] E.A. Bier, S.H. Robertson, G.M. Schrank, C. Rackley, J.G. Mammarappallil, S. Rajagopal, H.P. McAdams, B. Driehuys, A protocol for quantifying cardiogenic oscillations in dynamic (129) Xe gas exchange spectroscopy: the effects of idiopathic pulmonary fibrosis, NMR Biomed. 32 (2019) e4029.

[239] Z.I. Cleveland, G.P. Cofer, G. Metz, D. Beaver, J. Nouls, S.S. Kaushik, M. Kraft, J. Wolber, K.T. Kelly, H.P. McAdams, B. Driehuys, Hyperpolarized (129)Xe MR imaging of alveolar gas uptake in humans, PLoS ONE 5 (2010).

[240] S.S. Kaushik, M.S. Freeman, Z.I. Cleveland, J. Davies, J. Stiles, R.S. Virgincar, S.H. Robertson, M. He, K.T. Kelly, W.M. Foster, H.P. McAdams, B. Driehuys, Probing the regional distribution of pulmonary gas exchange through single-breath gas- and dissolved-phase 129 Xe MR imaging, J. Appl. Physiol. 115 (2013) 850–860.

[241] S.D. Swanson, M.S. Rosen, K.P. Coulter, R.C. Welsh, T.E. Chupp, Distribution and dynamics of laser-polarized (129)Xe magnetization in vivo, Magn. Reson. Med. 42 (1999) 1137–1145.

[242] W.T. Dixon, Simple proton spectroscopic imaging, Radiology 153 (1984) 189–194.

[243] S.S. Kaushik, S.H. Robertson, M.S. Freeman, M. He, K.T. Kelly, J.E. Roos, C.R. Rackley, W.M. Foster, H.P. McAdams, B. Driehuys, Single-breath clinical imaging of hyperpolarized129xe in the airspaces, barrier, and red blood cells using an interleaved 3D radial 1-point Dixon acquisition, Magn. Reson. Med. 75 (2016) 1434–1443.

[244] A.D. Hahn, J. Kammerman, S.B. Fain, Removal of hyperpolarized (129) Xe gas-phase contamination in spectroscopic imaging of the lungs, Magn. Reson. Med. 80 (2018) 2586–2597.

[245] S.B. Reeder, J.H. Brittain, T.M. Grist, Y.F. Yen, Least-squares chemical shift separation for 13C metabolic imaging, J. Magn. Reson. Imaging 26 (2007) 1145–1152.

[246] B. Zanette, G. Santyr, Accelerated interleaved spiral-IDEAL imaging of hyperpolarized (129) Xe for parametric gas exchange mapping in humans, Magn. Reson. Med. 82 (2019) 1113–1119.

[247] O. Doganay, T. Wade, E. Hegarty, C. McKenzie, R.F. Schulte, G.E. Santyr, Hyperpolarized (129) Xe imaging of the rat lung using spiral IDEAL, Magn. Reson. Med. 76 (2016) 566–576.

[248] J.M. Wang, S.H. Robertson, Z. Wang, M. He, R.S. Virgincar, G.M. Schrank, R.M. Smigla, T.G. O'Riordan, J. Sundy, L. Ebner, C.R. Rackley, P. McAdams, B. Driehuys, Using hyperpolarized 129 Xe MRI to quantify regional gas transfer in idiopathic pulmonary fibrosis, Thorax 73 (2017), thoraxjnl-2017-210070.

[249] L.J. Rankine, Z. Wang, J.M. Wang, M. He, H.P. McAdams, J. Mammarappallil, C. R. Rackley, B. Driehuys, R.M. Tighe, (129)Xenon gas exchange magnetic resonance imaging as a potential prognostic marker for progression of idiopathic pulmonary fibrosis, Ann. Am. Thorac. Soc. 17 (2020) 121–125.

[250] Z. Wang, E.A. Bier, A. Swaminathan, K. Parikh, J. Nouls, M. He, J.G. Mammarappallil, S. Luo, B. Driehuys, S. Rajagopal, Diverse cardiopulmonary diseases are associated with distinct xenon magnetic resonance imaging signatures, Eur. Respir. J. 54 (2019).

[251] Z. Wang, S.H. Robertson, J. Wang, M. He, R.S. Virgincar, G.M. Schrank, E.A. Bier, S. Rajagopal, Y.C. Huang, T.G. O'Riordan, C.R. Rackley, H.P. McAdams, B. Driehuys, Quantitative analysis of hyperpolarized 129Xe gas transfer MRI, Med. Phys. 44 (2017) 2415–2428.

[252] A.D. Hahn, J. Kammerman, M. Evans, W. Zha, R.V. Cadman, K. Meyer, N. Sandbo, S.B. Fain, Repeatability of regional pulmonary functional metrics of Hyperpolarized (129) Xe dissolved-phase MRI, J. Magn. Reson. Imaging 50 (2019) 1182–1190.

[253] A.L. Kern, M. Gutberlet, K. Qing, A. Voskrebenzev, F. Klimes, T.F. Kaireit, C. Czerner, H. Biller, F. Wacker, K. Ruppert, J.M. Hohlfeld, J. Vogel-Claussen, Regional investigation of lung function and microstructure parameters by localized (129) Xe chemical shift saturation recovery and dissolved-phase imaging: a reproducibility study, Magn. Reson. Med. 81 (2019) 13–24.

[254] O. Doganay, E. Stirrat, C. McKenzie, R.F. Schulte, G.E. Santyr, Quantification of regional early stage gas exchange changes using hyperpolarized 129 Xe MRI in a rat model of radiation-induced lung injury, Med. Phys. 43 (2016) 2410–2420.

[255] B. Zanette, E. Stirrat, S. Jelveh, A. Hope, G. Santyr, Physiological gas exchange mapping of hyperpolarized 129Xe using spiral-IDEAL and MOXE in a model of regional radiation-induced lung injury, Med. Phys. 45 (2018) 803–816.

[256] P.J. Niedbalski, E.A. Bier, Z. Wang, M.M. Willmering, B. Driehuys, Z.I. Cleveland, Mapping cardio-pulmonary dynamics within the microvasculature of the lungs using dissolved (129)Xe MRI, J. Appl. Physiol. (1985) (2020).

[257] K. Ruppert, J.R. Brookeman, K.D. Hagspiel, J.P. Mugler 3rd, Probing lung physiology with xenon polarization transfer contrast (XTC), Magn. Reson. Med. 44 (2000) 349–357.

[258] K. Ruppert, J.F. Mata, H.-T.J. Wang, W.A. Tobias, G.D. Cates, J.R. Brookeman, K. D. Hagspiel, J.P. Mugler, XTC MRI: sensitivity improvement through parameter optimization, Magn. Reson. Med. 57 (2007) 1099–1109.

[259] H. Imai, A. Kimura, Y. Hori, S. Iguchi, T. Kitao, E. Okubo, T. Ito, T. Matsuzaki, H. Fujiwara, Hyperpolarized 129Xe lung MRI in spontaneously breathing mice with respiratory gated fast imaging and its application to pulmonary functional imaging, NMR Biomed. 24 (2011) 1343–1352.

[260] I. Dregely, J.P. Mugler 3rd, I.C. Ruset, T.A. Altes, J.F. Mata, G.W. Miller, J. Ketel, S. Ketel, J. Distelbrink, F.W. Hersman, K. Ruppert, Hyperpolarized Xenon-129 gas-exchange imaging of lung microstructure: first case studies in subjects with obstructive lung disease, J. Magn. Reson. Imaging 33 (2011) 1052–1062.

[261] I. Dregely, I.C. Ruset, J.F. Mata, J. Ketel, S. Ketel, J. Distelbrink, T.A. Altes, J.P. Mugler, G.W. Miller, F.W. Hersman, K. Ruppert, Multiple-exchange-time xenon polarization transfer contrast (MXTC) MRI: initial results in animals and healthy volunteers, Magn. Reson. Med. 67 (2012) 943–953.

[262] M.S. Albert, D.F. Kacher, D. Balamore, A.K. Venkatesh, F.A. Jolesz, T(1) of (129) Xe in blood and the role of oxygenation, J. Magn. Reson. 140 (1999) 264–273.

[263] C.H. Tseng, S. Peled, L. Nascimben, E. Oteiza, R.L. Walsworth, F.A. Jolesz, NMR of laser-polarized 129Xe in blood foam, J. Magn. Reson. 126 (1997) 79–86.

[264] J. Wolber, A. Cherubini, M.O. Leach, A. Bifone, Hyperpolarized 129Xe NMR as a probe for blood oxygenation, Magn. Reson. Med. 43 (2000) 491–496.

[265] J. Astrup, B.K. Siesjo, L. Symon, Thresholds in cerebral ischemia – the ischemic penumbra, Stroke; J. Cerebral Circulat. 12 (1981) 723–725.

[266] S.H. Rahimtoola, The hibernating myocardium, Am. Heart J. 117 (1989) 211–221.

[267] K. Hoenderdos, A. Condliffe, The neutrophil in chronic obstructive pulmonary disease, Am. J. Respir. Cell Mol. Biol. 48 (2013) 531–539.

[268] G. Leung, G. Norquay, J. Parra-Robles, J.M. Wild, Measuring red blood cell oxygenation in vivo using hyperpolarized 129Xe MRI, Eur. Respir. J. 40 (2012) P2734.

[269] A.K. Venkatesh, K.S. Hong, Y. Kubatina, R.V. Sun, F.A. Mulkern, M.S. Jolesz, M.S. Albert, Direct observation of the transport of 129Xe from the Lung-gas to the tissue and the blood, Proc. Intl. Soc. Mag. Reson. (2001) 984.

[270] K. Ruppert, T.A. Altes, J.F. Mata, I.C. Ruset, F.W. Hersman, J.P. Mugler, Detecting pulmonary capillary blood pulsations using hyperpolarized xenon-129 chemical shift saturation recovery (CSSR) MR spectroscopy, Magn. Reson. Med. 75 (2016) 1771–1780.

[271] O.L. Wade, J.M. Bishop, Cardiac Output and Regional Blood Flow, Blackwell Scientific Publications, 1962.

[272] E. Kandel, J.H. Schwartz, T. Jessell, Principles of Neural Science, McGraw-Hill Medical, 2000.

[273] F.T. Hane, T. Li, J.-A. Plata, A. Hassan, K. Granberg, M.S. Albert, Inhaled Xenon Washout as a Biomarker of Alzheimer's Disease, Diagnostics 8 (2018) 41.

[274] J. Mugler, G. Miller, C. Meyer, K. Qing, J. Mata, S. Guan, Imaging of dissolved-phase hyperpolarized xenon-129 in human kidneys, Proc. Intl. Soc. Mag. Reson. Med. 23 (2015) 848.

[275] J. Kershaw, K. Nakamura, Y. Kondoh, A. Wakai, N. Suzuki, I. Kanno, Confirming the existence of five peaks in 129Xe rat head spectra, Magn. Reson. Med. 57 (2007) 791–797.

[276] M.A. Antonacci, L. Zhang, A. Burant, D. McCallister, R.T. Branca, Simple and robust referencing system enables identification of dissolved-phase xenon spectral frequencies, Magn. Reson. Med. 80 (2018) 431–441.

[277] S.S. Rengachary, R.G. Ellenbogen, Principles of Neurosurgery, Elsevier Mosby, 2005.

[278] J.S. Meyer, L.A. Hayman, M. Yamamoto, F. Sakai, S. Nakajima, Local cerebral blood-flow measured By CT after stable xenon inhalation, Am. J. Roentgenol. 135 (1980) 239–251.

[279] M.L. Mazzanti, R.P. Walvick, X. Zhou, Y. Sun, N. Shah, J. Mansour, J. Gereige, M. S. Albert, Distribution of hyperpolarized xenon in the brain following sensory stimulation: preliminary MRI findings, PLoS ONE 6 (2011) e21607.

[280] X. Zhou, Y. Sun, M. Mazzanti, N. Henninger, J. Mansour, M. Fisher, M. Albert, MRI of stroke using hyperpolarized 129Xe, NMR Biomed. 24 (2011) 170–175.

[281] M.R. Rao, G. Norquay, N.J. Stewart, N. Hoggard, P.D. Griffiths, J.M. Wild, Assessment of brain perfusion using hyperpolarized (129) Xe MRI in a subject with established stroke, J. Magn. Reson. Imaging 50 (2019) 1002–1004.

[282] M. Wintermark, M. Sesay, E. Barbier, K. Borbely, W.P. Dillon, J.D. Eastwood, T. C. Glenn, C.B. Grandin, S. Pedraza, J.F. Soustiel, T. Nariai, G. Zaharchuk, J.M. Caille, V. Dousset, H. Yonas, Comparative overview of brain perfusion imaging techniques, Stroke; J. Cerebral Circulat. 36 (2005) e83–e99.

[283] E. Ledneva, S. Karie, V. Launay-Vacher, N. Janus, G. Deray, Renal safety of gadolinium-based contrast media in patients with chronic renal insufficiency, Radiology 250 (2009) 618–628.

[284] R.J. McDonald, J.S. McDonald, D.F. Kallmes, M.E. Jentoft, D.L. Murray, K.R. Thielen, E.E. Williamson, L.J. Eckel, Intracranial gadolinium deposition after contrast-enhanced MR imaging, Radiology 275 (2015) 772–782.

[285] D.C. Alsop, J.A. Detre, X. Golay, M. Günther, J. Hendrikse, L. Hernandez-Garcia, H. Lu, B.J. Macintosh, L.M. Parkes, M. Smits, M.J.P. Van Osch, D.J.J. Wang, E.C. Wong, G. Zaharchuk, Recommended implementation of arterial spin-labeled Perfusion mri for clinical applications: a consensus of the ISMRM Perfusion Study group and the European consortium for ASL in dementia, Magn. Reson. Med. 73 (2015) 102–116.

[286] G. Miller, G. Cates, D. Keder, T. Altes, J. Mata, K. Qing, I. Ruset, F. Hersman, J. Mugler, Dynamic spectroscopy of dissolved-phase xenon-129 in the human kidney, Proc. Intl. Soc. Mag. Reson. Med. 25 (2017).

[287] J. Chacon-Caldera, A. Maunder, M. Rao, G. Norquay, O. Rodgers, M. Clemence, C. Puddu, S. Lothar, J.M. Wild, Dynamic MRI of hyperpolarized xenon-129 uptake in the human kidney using a dedicated transmission-only-reception-only array at 3 Tesla, Proc. Intl. Soc. Mag. Reson. Med. 26 (2018) P 4470.

[288] M. Notohamiprodjo, S. Sourbron, M. Staehler, H.J. Michaely, U.I. Attenberger, G.P. Schmidt, H. Boehm, A. Horng, C. Glaser, C. Stief, M.F. Reiser, K.A. Herrmann, Measuring perfusion and permeability in renal cell carcinoma with dynamic contrast-enhanced MRI: a pilot study, J. Magn. Reson. Imaging 31 (2010) 490–501.

[289] K.L. Wright, Y. Chen, H. Saybasili, M.A. Griswold, N. Seiberlich, V. Gulani, Quantitative high-resolution renal perfusion imaging using 3-dimensional through-time radial generalized autocalibrating partially parallel acquisition, Invest. Radiol. 49 (2014) 666–674.

[290] H. Marshall, A. Horsley, C.J. Taylor, L. Smith, D. Hughes, F.C. Horn, A.J. Swift, J. Parra-Robles, P.J. Hughes, G. Norquay, N.J. Stewart, G.J. Collier, D. Teare, S. Cunningham, I. Aldag, J.M. Wild, Detection of early subclinical lung disease in children with cystic fibrosis by lung ventilation imaging with hyperpolarised gas MRI, Thorax 72 (2017) 760–762.

[291] S.J. Kruger, D.J. Niles, B. Dardzinski, A. Harman, N.N. Jarjour, M. Ruddy, S.K. Nagle, C.J. Francois, R.L. Sorkness, R.M. Burton, A. Munoz del Rio, S.B. Fain, Hyperpolarized Helium-3 MRI of exercise-induced bronchoconstriction during challenge and therapy, J. Magn. Reson. Imaging 39 (2014) 1230–1237.

[292] T.A. Altes, M. Johnson, M. Fidler, M. Botfield, N.J. Tustison, C. Leiva-Salinas, E. E. de Lange, D. Froh, J.P. Mugler 3rd, Use of hyperpolarized helium-3 MRI to assess response to ivacaftor treatment in patients with cystic fibrosis, J. Cyst. Fibros. 16 (2017) 267–274.

[293] S.B. Fain, G. Gonzalez-Fernandez, E.T. Peterson, M.D. Evans, R.L. Sorkness, N.N. Jarjour, W.W. Busse, J.E. Kuhlman, Evaluation of structure-function

relationships in asthma using multidetector CT and hyperpolarized He-3 MRI, Acad. Radiol. 15 (2008) 753–762.

[294] S. Svenningsen, E. Haider, C. Boylan, M. Mukherjee, R.L. Eddy, D.P.I. Capaldi, G. Parraga, P. Nair, CT and functional MRI to evaluate airway mucus in severe asthma, Chest 155 (2019) 1178–1189.

[295] L.J. Rankine, Z. Wang, B. Driehuys, L.B. Marks, C.R. Kelsey, S.K. Das, Correlation of regional lung ventilation and gas transfer to red blood cells: implications for functional-avoidance radiation therapy planning, Int. J. Radiat. Oncol. Biol. Phys. 101 (2018) 1113–1122.

[296] K. Qing, N.J. Tustison, J.P. Mugler 3rd, J.F. Mata, Z. Lin, L. Zhao, D. Wang, X. Feng, J.Y. Shin, S.J. Callahan, M.P. Bergman, K. Ruppert, T.A. Altes, J.M. Cassani, Y.M. Shim, Probing changes in lung physiology in COPD using CT, perfusion MRI, and hyperpolarized xenon-129 MRI, Acad. Radiol. 26 (2019) 326–334.

[297] M. He, Z. Wang, L. Rankine, S. Luo, J. Nouls, R. Virgincar, J. Mammarappallil, B. Driehuys, Generalized linear binning to compare hyperpolarized (129)Xe ventilation maps derived from 3D radial gas exchange versus dedicated multislice gradient echo MRI, Acad. Radiol. (2019).

[298] G. Mussell, H. Marshall, L. Smith, A. Biancardi, P.J.C. Hughes, A. Swift, G. Collier, J.M. Wild, I. Sabroe, Correlations of Ventilation Heterogeneity and Spirometry in Asthma; Initial Experience with Hyperpolarised Gas MRI in a Clinical Setting, European Respiratory Society, Madrid, 2019, p. 3163.

[299] E.A. Bier, J.C. Nouls, Z. Wang, M. He, G. Schrank, N. Morales-Medina, R. Hashoian, H. Svetlik, J.P. Mugler 3rd, B. Driehuys, A thermally polarized (129) Xe phantom for quality assurance in multi-center hyperpolarized gas MRI studies, Magn. Reson. Med. 82 (2019) 1961–1968.

[300] H.E. Moller, X.J. Chen, B. Saam, K.D. Hagspiel, G.A. Johnson, T.A. Altes, E.E. de Lange, H.U. Kauczor, MRI of the lungs using hyperpolarized noble gases, Magn. Reson. Med. 47 (2002) 1029–1051.

[301] H.U. Kauczor, R. Surkau, T. Roberts, MRI using hyperpolarized noble gases, Eur. Radiol. 8 (1998) 820–827.

[302] R. Seydoux, P. Diehl, R.K. Mazitov, J. Jokisaari, Chemical-shifts in magnetic-resonance of the 3He nucleus in liquid solvents and comparison with other noble gases, J. Magn. Reson., Ser A 101 (1993) 78–83.

[303] J.H. Wang, Self-diffusion coefficients of water, J. Phys. Chem. 69 (1965), 4412–4412.

[304] M.S. Albert, V.D. Schepkin, T.F. Budinger, Measurement of 129Xe T1 in blood to explore the feasibility of hyperpolarized 129Xe MRI, J. Comput. Assist. Tomogr. 19 (1995) 975–978.

[305] J. Wolber, D.J. McIntyre, L.M. Rodrigues, P. Carnochan, J.R. Griffiths, M.O. Leach, A. Bifone, In vivo hyperpolarized 129Xe NMR spectroscopy in tumors, Magn. Reson. Med. 46 (2001) 586–591.

[306] J. Wolber, I.J. Rowland, M.O. Leach, A. Bifone, Perfluorocarbon emulsions as intravenous delivery media for hyperpolarized xenon, Magn. Reson. Med. 41 (1999) 442–449.

[307] J.C. Woods, C.K. Choong, D.A. Yablonskiy, J. Bentley, J. Wong, J.A. Pierce, J.D. Cooper, P.T. Macklem, M.S. Conradi, J.C. Hogg, Hyperpolarized 3He diffusion MRI and histology in pulmonary emphysema, Magn. Reson. Med. 56 (2006) 1293–1300.

[308] D.A. Yablonskiy, A.L. Sukstanskii, J.D. Quirk, J.C. Woods, M.S. Conradi, Probing lung microstructure with hyperpolarized noble gas diffusion MRI: theoretical models and experimental results, Magn. Reson. Med. 71 (2014) 486–505.

[309] J.R. Birchall, R.K. Irwin, P. Nikolaou, A.M. Coffey, B.E. Kidd, M. Murphy, M. Molway, L.B. Bales, K. Ranta, M.J. Barlow, B.M. Goodson, M.S. Rosen, E.Y.XeUS Chekmenev, A second-generation automated open-source batch-mode clinical-scale hyperpolarizer, J. Magn. Reson. 319 (2020) 106813.

[311] N.Y. Lin, D.J. Roach, M.M. Willmering, L.L. Walkup, M.M. Hossain, P. Desirazu, Z.I. Cleveland, T.W.J.C. Guilbert, Woods, (129)Xe MRI as a measure of clinical disease severity for pediatric asthma, J. Allergy. Clin. Immunol. (2020).

[312] C.S. Hall, J.D. Quirk, C.W. Goss, D. Lew, J. Kozlowski, R.P. Thomen, J.C. Woods, N.J. Tustison, J.P. Mugler 3rd, L. Gallagher, T. Koch, K.B. Schechtman, I.C. Ruset, F.W. Hersman, M. Castro, Single-Session Bronchial Thermoplasty Guided by (129)Xe Magnetic Resonance Imaging. A Pilot Randomized Controlled Clinical Trial, Am. J. Respir.. Crit. Care Med. 202 (2020) 524–534.

[313] L.J. Smith, H. Marshall, J. Bray, M. Wildman, N. West, A. Horsley, J.M. Wild, The effect of acute maximal exercise on the regional distribution of ventilation using ventilation MRI in CF, J. Cyst. Fibros. (2020).

[314] L.J. Smith, A. Horsley, J. Bray, P.J.C. Hughes, A. Biancardi, G. Norquay, M. Wildman, N. West, H. Marshall, J.M. Wild, The assessment of short and long term changes in lung function in CF using (129)Xe MRI, Eur. Respir J. (2020).

[315] S. Tafti, W.J. Garrison, J.P. Mugler, 3rd, Y.M. Shim, T.A. Altes, J.F. Mata, E.E. de Lange, G.D. Cates, Jr., A.M. Ropp, C. Wang, G.W. Miller, Emphysema Index Based on Hyperpolarized (3)He or (129)Xe Diffusion MRI: Performance and Comparison with Quantitative CT and Pulmonary Function Tests, Radiology, 297 (2020) 201-210.

[316] P.J. Niedbalski, A.S. Cochran, M.S. Freeman, J. Guo, E.M. Fugate, C.B. Davis, J. Dahlke, J.D. Quirk, B.M. Varisco, J.C. Woods, Z.I. Cleveland, Validating in vivo hyperpolarized (129) Xe diffusion MRI and diffusion morphometry in the mouse lung, Magn. Reson. Med. (2020).

[317] K. Ruppert, F. Amzajerdian, Y. Xin, H. Hamedani, L. Loza, T. Achekzai, I.F. Duncan, H. Profka, Y. Qian, M. Pourfathi, S. Kadlecek, R.R. Rizi, Investigating biases in the measurement of apparent alveolar septal wall thickness with hyperpolarized 129Xe MRI, Magn. Reson. Med. (2020).

[318] G.J. Collier, J.A. Eaden, P.J.C. Hughes, S.M. Bianchi, N.J. Stewart, N.D. Weatherley, G. Norquay, R.F. Schulte, J.M. Wild, Dissolved (129) Xe lung MRI with four-echo 3D radial spectroscopic imaging: Quantification of regional gas transfer in idiopathic pulmonary fibrosis, Magn. Reson. Med. (2020).

[319] Rao M.R., Norquay G., Stewart N.J., Wild J.M., Measuring 129Xe transfer across the blood brain barrier using magnetic resonance spectroscopy, Magnetic Resonance in Medicine, doi:10.1002/mrm.28646.

[320] H. Li, X. Zhao, Y. Wang, X. Lou, S. Chen, H. Deng, L. Shi, J. Xie, D. Tang, J. Zhao, L. S. Bouchard, L. Xia, X. Zhou, Damaged lung gas-exchange function of discharged COVID-19 patients detected by hyperpolarized (129)Xe MRI, Sci Adv (2020).

Glossary

ADC: apparent diffusion coefficient
B_0: main magnetic field
B_1+: transmit magnetic field
CF: cystic fibrosis
CF-SEOP: continuous flow spin exchange optical pumping
COPD: chronic obstructive pulmonary disease
CSI: chemical shift imaging
CSSR: chemical shift saturation recovery
CT: computed tomography
D: diffusivity
DDC: distributed diffusivity coefficient
D_L: longitudinal diffusion coefficient
D_0: free diffusion coefficient
D_T: transverse diffusion coefficient
FID: free induction decay
FLORET: Fermat Looped ORthogonally Encoded Trajectories
FRC: functional residual capacity
FVC: forced vital capacity
h: alveolar sleeve depth
^1H: proton
^3He: helium-3
HP: hyperpolarised
IDEAL: iterative decomposition with echo asymmetric and least-squares estimation
ILD: interstitial lung disease
IPF: idiopathic pulmonary fibrosis
LHF: left heart failure
Lm: mean linear intercept
Lm_D: mean diffusion length scale
MR: magnetic resonance
MRI: magnetic resonance imaging
MRS: magnetic resonance spectroscopy
MXTC: multiple exchange time xenon polarisation transfer contrast
N_2: nitrogen
NMR: nuclear magnetic resonance
PAH: pulmonary arterial hypertension
pO_2: partial pressure of oxygen
Q_{coil}: coil quality factor
R: outer acinar airway radii
Rb: rubidium
RBC: red blood cell
RF: radiofrequency
S_{Alv}: alveolar surface area
SEOP: spin exchange optical pumping
SF-SEOP: stopped flow spin exchange optical pumping
SNR: signal to noise ratio
sO_2: blood oxygenation
SPECT: single photon emission tomography
SPGR: spoiled gradient echo
S/V: surface area to volume ratio
T_1: longitudinal relaxation time
T_{2*}: transverse relaxation time
TLC: total lung capacity
T_{LCO}: transfer coefficient for carbon monoxide
TP: tissue-plasma
TR: repetition time
UTE: ultra short echo time
V_{Alv}: alveolar volume
VDP: ventilation defect percentage
VV%: ventilated volume percentage
ω: resonant frequency
^{129}Xe: xenon-129
XTC: xenon polarisation transfer contrast